Christoph Zambanini, BSc

Landslides triggered in the Rasuwa, Nuwakot and Dhading Districts (Nepal) during the M 7.8 Gorkha (Nepal) Earthquake of April 25, 2015

MASTER'S THESIS

to achieve the university degree of

Master of Science

Master's degree programme: Earth Sciences

submitted to

Graz University of Technology

Supervisor

Univ.-Prof. B.A. M.Sc. Ph.D. Daniel Scott Kieffer

Institute of Applied Geoscience

Graz, January 2018

AFFIDAVIT

I declare that I have authored this thesis independently, that I have not used other than the declared sources/resources, and that I have explicitly indicated all material which has been quoted either literally or by content from the sources used. The text document uploaded to TUGRAZonline is identical to the present master‘s thesis.

Date

Signature

Acknowledgment:

First of all, I would like to thank my supervisor Scott Kieffer for giving me the opportunity to make such an interesting master thesis. I would like to thank him for the very informative and also exciting time in Nepal, for the discussions and the time he spent to meet with me and the other interesting projects I became involved through him.

Secondly, I want to thank Maja Bitec for her passion and patience by helping me with questions about QGIS, Google Earth Pro and the entire thesis. It was a pleasure working with Maja in the laboratory.

I would like to thank Mirjam Ziselsberger, who worked on the same topic in her thesis except that she covered the neighboring Sindhupalchok district. I want to thank Mirjam for the discussions and the ideas regarding the thesis and for the nice time in Nepal.

Next, I have to thank Surendra Awasthi from Nepal for supporting us during our field work. He provided us with information, maps and everything else needed for the trip.

A very important issue for me is to thank my family. First of all I want to thank my parents Andreas and Christine for supporting me over my whole studying time and my whole life. It is not given that parents support you as much as they do. Also, I would like to thank my brother Johannes for interesting discussions over the whole study time and eventually bringing me to the idea of studying geology.

My dearest Eva, I do not know how to thank you for supporting me that much. Not only correcting my whole thesis more than once, also bringing me to smile, knowing when I need rest even when I don't and just supporting me in every way you can including all my travelling. I know it was not easy all the time, thank you for your support. You gave me the energy to do this thesis beside all the other projects and organizations I am/was involved and have/had to make.

Last but not least I want to thank all my friends, who made my free time as great and enjoyable as possible.

Contents

List of Figures

List of Tables

Abstract

The Gorkha (Nepal) earthquake of April 25, 2015, with a magnitude of 7.8 M_w, has been the largest earthquake in this area since 1934. Approximately 8800 people were killed during the earthquake, tens of thousands of people were injured and hundreds of thousands of buildings were destroyed. Thousands of landslides were triggered, destroying roads and villages or blocking roads and rivers (Hashash et al., 2015).

Due to the fact that landslides occur where they have previously occurred or in similar conditions, it is important to make an earthquake triggered landslide inventory including all the geomorphometric and spatial landslide specific parameters. To generate this inventory for the three districts Rasuwa, Nuwakot and Dhading, mapping on high resolution Google Earth Pro satellite imagery, combined with QGIS, Excel and R Studio was performed. For each of the detected and by the earthquake activated landslide (in total 8330), the location, surface area, slope angle, aspect ratio, geologic unit, slope aspect, slope relief, elevation, distance to epicenter and ground slip magnitude was determined. Besides, information about affected infrastructure (roads or villages) and whether the landslide was earthquake induced or pre – existing but reactivated was collected. These datasets were statistically analyzed and plotted as diagrams or maps. Further, a map was created including the landslide density and the peak ground acceleration (PGA) (Earthquake Damage Analysis Center, 2015a).

The data evaluation shows that there are four major factors which influenced the susceptibility for landsliding. The first is the ground slip magnitude, which has the highest landslide density between the values of 3.0 m and 5.0 m. Because of the predominantly flat topography in areas of high ground slip magnitudes, the landslide density decreases at the highest magnitudes. The second parameter is the slope angle. The highest landslide susceptibility was located at slope angles of 55° - 60° even though the most present slope angle of the research area was at 25° - 30°. The third factor was the geology. The Augen gneisses and mica granites occurring in the Kuncha Group and Nawakot Group and the mainly shallow marine sediments of the Kuncha Group had by far the highest landslide density. This effect is thought to be due to structural, textural and weathering properties. The forth factor is the slope aspect. A distinct trend of landslides occurring preferably on south and west facing slopes was present. Some authors explain this trend by various factors which can increase the susceptibility of the slope for landsliding already before the earthquake occurs by effecting the vegetation, the weathering, the degree of saturation or the rock mass strength (e.g. Guzzetti et al., 1999; Evans et al., 1999; Nagarajan et al., 2000; Yalcin, 2008). These factors include exposure to sunlight, drying winds, rainfall and discontinuities. Additionally, the ground slip direction can have an influence too. To define the reliability of the data evaluation and to determine the effects of the monsoon on the landslides and the landslide conditions, two week of field reconnaissance were undertaken. This reconnaissance showed a high correlation of the dataset with the actual site conditions. The effect of the monsoon was determined as extreme. It already reshaped the landslides and activated new ones.

Based on this landslide inventory, earthquake triggered landslide hazard and risk assessments can be performed including hazard maps. Implementation of this dataset into a greater inventory can contribute to the development of detailed hazard assessment campaigns on a regional scale.

Kurzfassung

Das Gorkha (Nepal) Erdbeben des 25. April 2015 war mit einer Magnitude von 7,3 M_W in dieser Region das größte seit 1934. Dieses Erdbeben brachte ungefähr 8800 Menschen ums Leben, führte zu zehntausenden Verletzten und zu hunderttausenden zerstörten Gebäuden. Tausende Erdrutsche wurden ausgelöst, welche wiederum Straßen und Dörfer zerstörten oder Straßen und Flüsse blockierten (Hashash et al., 2015).

Da Hangrutschungen dort auftreten, wo sie bereits aufgetreten sind oder zumindest bei ähnlichen Gegebenheiten, ist es wichtig, Inventare mit allen geomorphologischen und hangrutschungs-spezifischen Daten über die von Erdbeben ausgelösten Hangrutschungen zu erstellen. Um für die drei Bezirke Rasuwa, Nuwakot und Dhading ein solches zu erstellen wurde eine Kartierung mit Hilfe von hochauflösenden Google Earth Pro Satellitenbildern gemeinsam mit QGIS, Excel und R Studio durchgeführt. Für jede erfasste und durch das Erdbeben ausgelöste Hangrutschung (gesamt 8330), wurden Daten über Position, Fläche, Meereshöhe, Hangneigung, Querschnittsverhältnis, geologische Einheit, Exposition, Hanghöhe, Distanz zum Epizentrum und Bodenversatz ermittelt. Zusätzlich wurden evaluiert, ob die Hangrutschung Infrastruktur beeinflusste und ob diese Hangrutschung erdbebeninduziert ist oder zuvor schon existierte und reaktiviert wurden. Diese Daten wurden sowohl in Diagrammen als auch in Karten visualisiert. Eine weitere erstellte Karte enthielten die Erdrutschdichte und die maximalen Bodenbeschleunigungskarte (PGA map).

Die Datenauswertung zeigt, dass tendenziell vier Faktoren das Auftreten von Hangrutschungen am meisten beeinflussten. Der erste Faktor ist der Bodenversatz, welcher die höchste Hangrutschungs-dichte zwischen einem Wert von 3,0 m und 5,0 m aufweist. Aufgrund von überwiegend flacher Topografie bei den höchsten Bodenversätzen, fällt die Hangrutschungsdichte an diesen Stellen. Der zweite Parameter ist die Hangneigung. Es zeigte sich, dass die höchste Hangrutschungsdichte auf Hängen mit einer Hangneigung von 55° -°60° ist, obwohl die flächenmäßig am häufigsten vorkommende Hangneigung des untersuchten Gebiets bei 25° - 30° liegt. Der dritte Einflussfaktor ist die geologische Einheit. Die Augengneisse und Glimmergranite der Kuncha Gruppe und der Nawakot Gruppe sowie die flachmarinen Sedimenten der Kuncha Gruppe weisen bei weitem die höchste Hangrutschungsdichte auf. Dieser Effekt ist auf strukturelle und textuelle, sowie verwitterungstechnischen Eigenschaften zurückzuführen. Der vierte Einflussfaktor ist die Hangexposition. Bei weitem die höchste Hangrutschungsdichte tritt auf südlich und westlich orientierten Hängen auf. Einige Autoren erklären Trends wie diesen mit verschiedene Faktoren, die durch Einflussname auf die Vegetation, die Verwitterung, die Sättigung oder die Gebirgsfestigkeit die Anfälligkeit des Hanges für Hangrutschungen schon vor dem Erdbeben erhöht (e.g. Guzzetti et al., 1999; Evans et al., 1999; Nagarajan et al., 2000; Yalcin, 2008). Zu diesen Faktoren gehören die Sonneneinstralung, Trocknungswinde, Regen und Trennflächenorientierung. Zudem kann die Bodenversatzrichtung einen Einfluss haben. Um die Zuverlässigkeit der Fernerkundungsdaten zu evaluieren und die Auswirkung des Monsoons auf die Hangrutschungen und die Faktoren bezüglich Hangrutschungen zu beurteilen, wurde eine zweiwöchige Erkundung der Gegebenheiten vor Ort durchgeführt. Diese zeigte eine hohe Korrelation der Fernerkundungsdaten mit den tatsächlichen Gegebenheiten. Der Effekt des Monsuns wurde als extrem eingestuft, da er die vorhandenen Hangrutschungen bereits verformte und weitere auslöste.

Durch Verwendung dieses Inventars können Gefahrenbeurteilungen wie Gefahrenkarten für von Erdbeben ausgelöste Hangrutschungen erstellt werden. Das Hinzufügen dieses Datensatzes zu anderen Inventaren kann dazu beitragen, detaillierte Gefahrenbeurteilungskampagnen zu erstellen.

1 Introduction

On April 25 2015, a M_W 7.8 earthquake hit Nepal. This earthquake resulted from a rupture of the Main Himalayan Thrust. The epicentral position of the earthquake was at 28.1473° N and 84.7079° E (USGS ANSS catalog). This earthquake killed approximately 8800 people, injured tens of thousands and destroyed hundreds of thousands of buildings. Additionally, thousands of landslides were triggered by this earthquake.

This study has been undertaken to document earthquake triggered landslides in three of the most strongly affected districts of Nepal, namely Rasuwa, Nuwakot and Dhading. The developed landslide inventory provides insights into dynamic slope processes and can be used for future landslide risk assessment in this area. To better understand factors controlling the distribution of earthquake induced landslides, a statistical analysis of various landslide attributes was performed in a GIS framework. Further on, a field reconnaissance was undertaken to evaluate the liability of the data combined with the evaluation of the effect of the monsoon on the landslides and the landslide conditions.

The thesis is subdivided into the following chapters:

1. **Introduction**: summarizes the purpose and the scope of the work. It also displays the structure of the thesis
2. **Regional Site Conditions:** provides a short overview of the geographical, geological, seismotectonical, seismological and landsliding conditions of Nepal
3. **Investigation Methods:** describes the used computer programs, the data analyzing methods, the field reconnaissance and the generated maps
4. **Data Analysis and Interpretation:** displays and describes the results of the data analyzation, including specially analyzed areas of intense landsliding, maps and field reconnaissance
5. **Discussion and Conclusion:** summarizes and interprets the results of the investigation
6. **References**

2 Regional Site Conditions

2.1 Geographical

Nepal is a landlocked country in Asia, situated between India and China. It has a total area of 147,181 km², a population of almost 26.5 million people and a population density of 180 people per km² (Bhusal, 2012). Its landscape is strongly shaped by topographic differences, which is also represented by its extreme elevation differences from 59 meters at the Indian border to 8,848 meters at the Mount Everest.

Rasuwa is a district directly at the Chinese border (Fig. 1). With 43,300 inhabitants (Bhusal, 2012), an area of 1,544 km² and a population density of 28 inhabitants per km² it is the least populated but second biggest of the observed districts (Bhusal, 2012). The district itself is mostly mountainous and consequently highly vulnerable to landsliding.

Nuwakot is bordering Rasuwa to the south (Fig 1). It has 277,471 inhabitants, an area of 1,121km² and 248 inhabitants per km² (Bhusal, 2012). As the district is south of Rasuwa and generally Nepal flattens towards the south, it is less mountainous and therefore has a higher population density. This leads to a much lower susceptibility of landslides to occur compared to Rasuwa.

The Dhading district extends from the mountainous terrain in the north to an even lower elevated area than Nuwakot. Dhading has 336,067 inhabitants (Bhusal, 2012), an area of 1,926km² and a population density of 174 inhabitants per km². The landslide density also lies between the two of Rasuwa and Nuwakot.

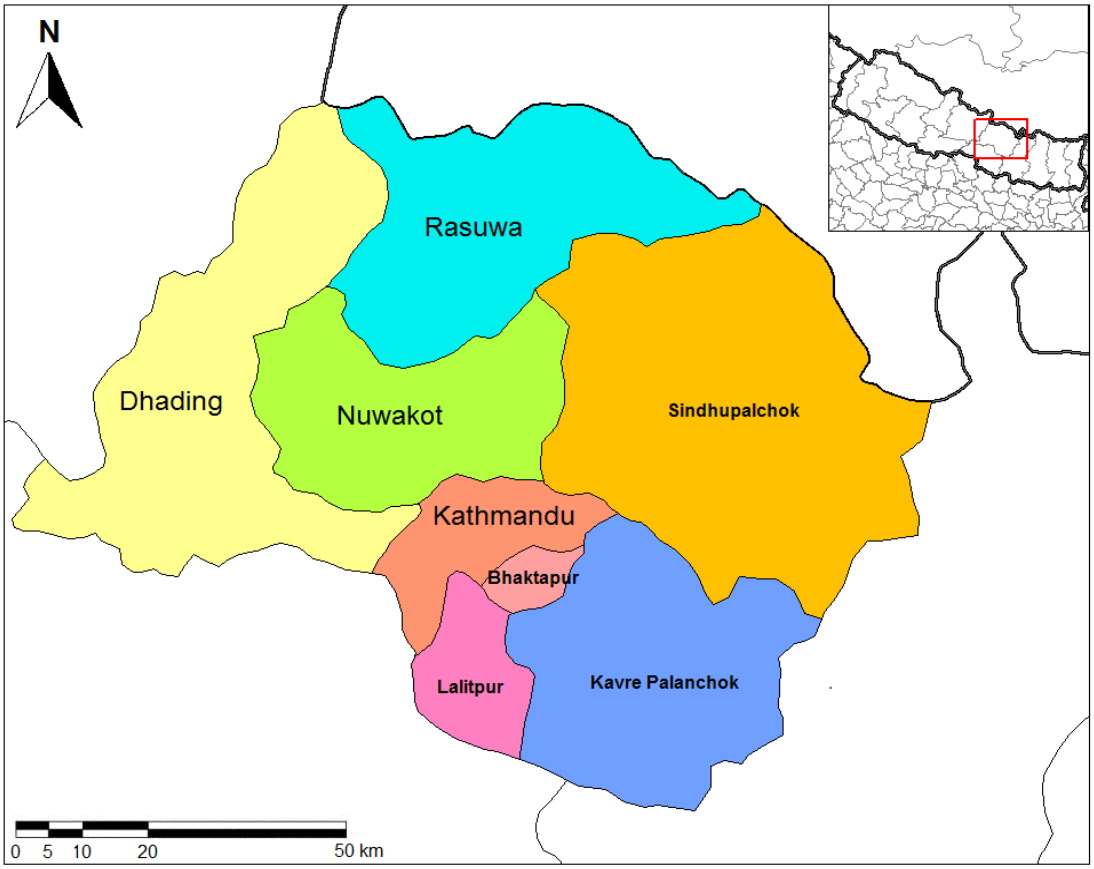

Fig. 1 Districts of Bagmati, Nepal, showing the three observed districts Rasuwa, Nuwakot and Dhading and Kathmandu, the capital of Nepal (Wikipedia).

2.2 Geological

The Himalaya mountain range stretches over 2,500 km and is the highest orogen on our planet (Le Fort, 1975). It was shaped by the continent – continent collision between the Indian and the Eurasian plate, approximately 52 Ma ago (e.g. Powell and Conaghan, 1973, Rowley, 1996; Searle et al., 1997). This collision lead to an obduction of the Indus – Tsangpo suture zone. After the collision, the Indian plate did not stop converging, metamorphism ensured and the Himalaya and the Tibetan plateau uplifted. Starting to uplift 20 Ma ago, the Himalaya and the Tibetan plateau obtained its present height only since between 2.5 Ma and 1.8 Ma ago (Powell & Conaghan 1973). Because of a too thick lithosphere at the Indus – Tsangpo suture zone, the pressure adjustment happened to the weaker gneiss and schist formations of the Himalayan area (Le Forte 1975). This allowed a double layer continental crust but also required further isostatic adjustment of approximately 5 km (Powell & Conaghan 1973).

The collision of India and Eurasia in addition to the resulting uplift of the Himalaya and the Tibetan plateau created a large number of tectonic faults. In the west of the Himalaya, the main sinistral Chaman fault and in the other cardinal direction the dextral Sagaing fault formed (Fig. 2). In the Himalaya itself the Main Central Thrust (MCT), the Main Boundary Thrust (MBT) and the Main Frontal Thrust (MFT) established (Fig. 3). The MCT runs through all three districts of the investigated area. Furthermore, many faults in central Asia were formed due to the escape movements of the Tibetan plateau to the east, caused by its huge uplift. Examples are the Altyn Tagh and Karakorus fault. All of these faults are known for generating earthquakes.

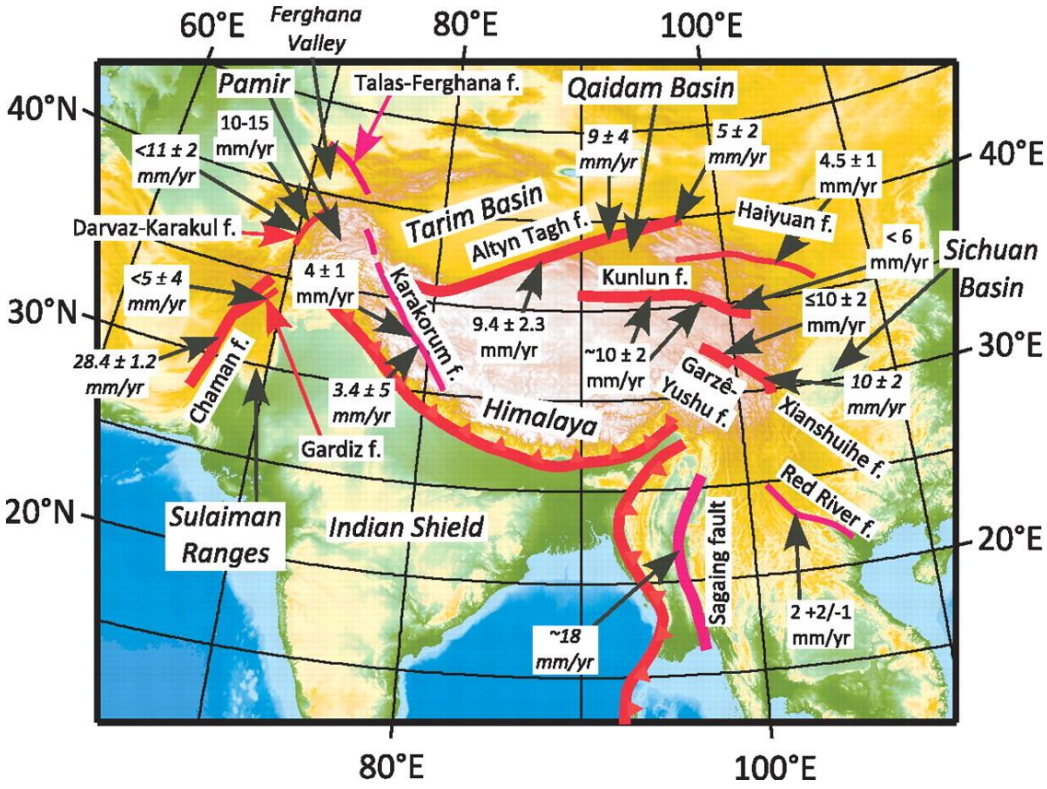

Fig. 2: Map of eastern Asia showing the traces of the Chaman, Darvaz-Karakul, Talas-Ferghana, Altyn Tagh, Karakorum, Kunlun, Haiyuan, Xianshuihe, Red River, and Sagaing faults (f.); rates for each are shown. Rates in italics are based on geodetic measurements. Purple lines show right-lateral faults, and red lines show left-lateral faults (Peter Molnar and Katherine E. Dayem Geosphere 2010, v. 6, p 444-467).

The three major east-west trending thrust faults in the Himalaya are boundaries between strong differences in geology.

The Sub Himalaya, the area called between the MFT (south) and the MBT (north) consists of the Siwalik Hills (Fig. 3b) (e.g., Delcaillau, 1986; Mugnier et al., 1999; Lave´ and Avouac, 2000). The Sub Himalaya consists of tertiary siltstones, sandstones and conglomerates with a thickness of several kilometers. This material is easily erodible and gets eroded by the highly erosive drainages originating in the Himalaya. The Siwalik Hills are characterized by low elevation hills with steep slopes (Hashash et al. 2015).

The Lesser Himalaya is located north of the MBT and south of the MCT (Fig. 3). The geology consists mainly of folded, medium to low-grade metasediments. These were deposited between ~ 16 to 21 Ma ago in the foreland of the Himalaya, before the uplift of the whole area (DeCelles et. al., 2001). The geomorphology is dominated by sharp reliefs with relatively low elevations (Hashash et al. 2015).

North of the MCT is the High or Greater Himalaya, with its high-grade metamorphic units composed of highly metamorphosed, amphibolite-grade schist and intrusive granitic plutons (Fig. 3). The elevation ranges from around 1000 to 8000 m, including the Mount Everest with 8848 m. The MCT is easily recognized by an abrupt break-in-slope, also defining the border between the Lesser and Higher Himalaya (Hashash et al., 2015).

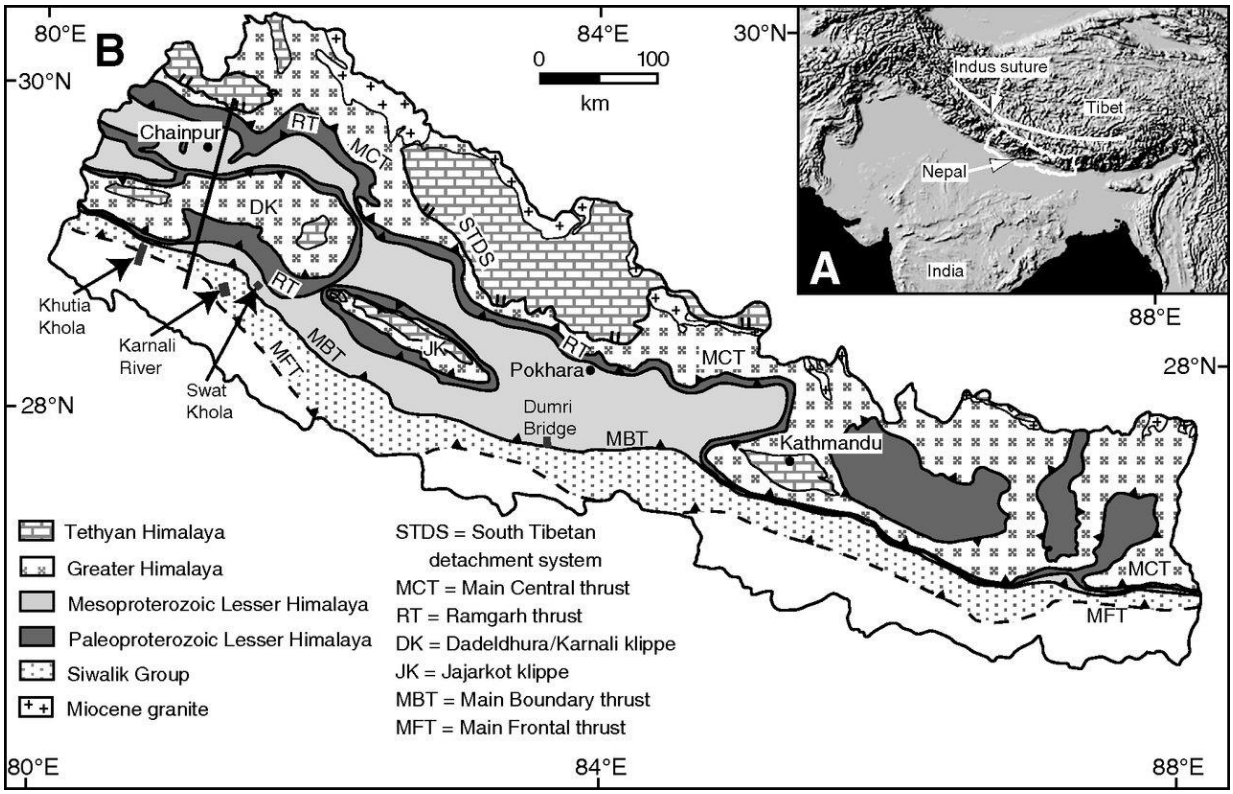

Fig. 3: (a) Digital image of the Tibetan Plateau and Himalayan thrust belt (from the Global 30 Arc Second Elevation Data Set). Nepal is outlined in white for reference (Robinson d. M. and Pearson O. N., 2006), (b) Tectonostratigraphic map of Nepal modified from Robinson et al. (2001). Geology of Kumaon, India (modified from Johnson, 2005).

2.3 Seismotectonic

The Indian plate is still converging towards the Eurasian plate, and therefore the tectonic regime is still active and generates high rates of seismicity. The northward convergence of India towards Eurasia is estimated at 40-50 mm/year (Patriat and Achache, 1984). Nearly half of this convergence is absorbed by plate boundary decollement and the other half is absorbed by crustal shortening (Avouac, 2003, Hashash et al., 2015).

Geophysical and structural studies lead to the assumption that the three major thrust faults in the Himalaya, namely the MFT, the MBT and the MCT (from south to north), merge into a single thrust fault at depth, the Main Himalayan Thrust fault (MHT) (Fig. 4). Under this thrust fault, the Indian plate is subducted underneath the Eurasian plate (Seeber and Armbruster, 1981; DeCelles et al., 2002; Bollinger, Henry and Avouac, 2006). Since the collision of India and Eurasia, the surface expression of the MHT has migrated southward. The first active thrust ramp was the MCT, the next the MBT and finally the MFT was produced by ongoing convergence and structural stacking at depth (e.g., Gansser, 1964; Le Fort, 1975; Nakata, 1989; Yeats et al., 1992).

The MHT has a flat-ramp-flat thrust geometry, which is sketched in Fig. 4. The upper flat part of it is locked and generates earthquakes, the ramp itself is a transition zone and the lower flat part is creeping. Interseismical studies by Ader (2012) showed that the incline of the MHT is very shallow and typically 5° to 6° in the flat parts and less than 10° at the ramp. This geometry produces earthquakes, which can be categorized in three different types: 1) Moderate earthquakes (in vicinity of the ramp); 2) Large blind earthquakes (1805, 1833, possibly 1905) which rupture from the top of the ramp to the MFT, without extending to the surface; and 3) Great earthquakes (1934, 1505, 1400, 1255, possibly 1100), which extend to the surface and likely down the ramp (Hashash et al., 2015). It is believed that the 1934 Bihar Nepal earthquake ruptured the MHT to the south of Kathmandu, similar to the 2015 Gorkha earthquake, but the Bihar-Nepal earthquake also ruptured the ground surface along the MFT, which the 2015 Gorkha earthquake did not do (Bollinger, et al., 2014). As a consequence, the 2015 Gorkha earthquake is categorized as type 2 and the 1934 Bihar Nepal earthquake as type 3 (Hashash et al., 2015). Bollinger et al. (2014) and others have documented evidence of a trend in this region, that only earthquakes with an $M > 8$ rupture the surface. This trend is consistent with the documented earthquakes of 1934 and 1255, which ruptured the surface, and the earthquakes of 1803, 1905 and 2015, which have not (Bollinger et al., 2014).

Generally the MHT and MFT are known to accommodate most of the crustal shortening, which is estimated between 17.3 and 23 mm/year (Larson et al., 1999, Ader, 2012, Bettinelli et al., 2006, Cattin and Avouac, 2000; Lave and Avouac, 2000; Bollinger, Henry, and Avouac, 2006). In contrast the MCT and MBT have only shown to be active in the east and west of the central Himalaya (Larson et al., 1999; Cattin and Avouac, 2000; Lave and Avouac, 2000; Bollinger, Henry, and Avouac, 2006).

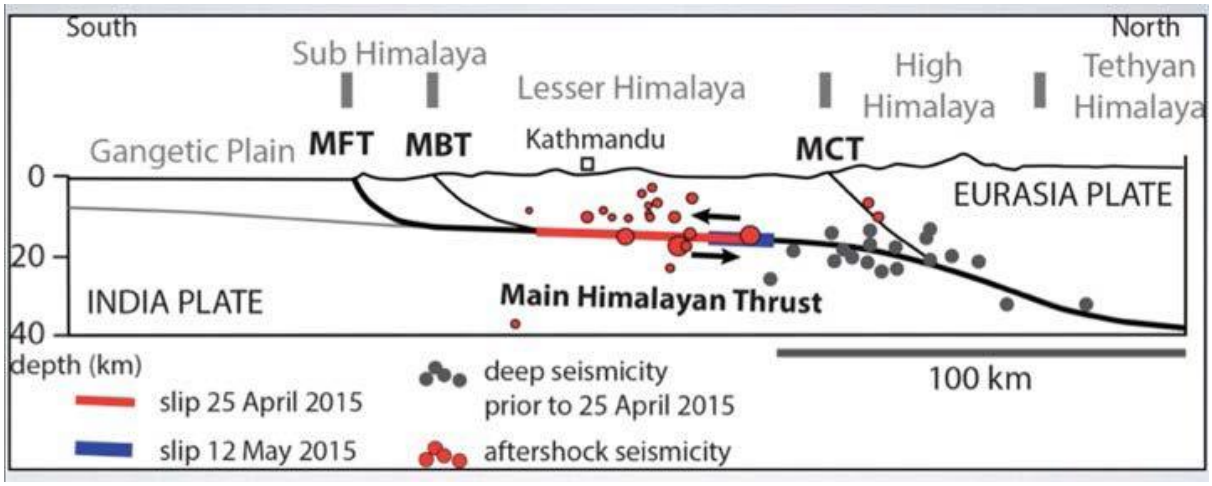

Fig. 4: Generalized cross section through the Central Himalaya showing the flat-ramp-flat geometry of the MHT and the modelled slip of the Gorkha earthquake and May 12, 2015 aftershock (Hashash et al., 2015; modified after USGS, 2015).

2.4 Seismological

The main thrust faults (MCT, MBT, MFT, and MHT) generate many earthquakes, affecting millions of people in the mountainous region of Nepal and India. Many historical earthquake damages have been recorded, but not their earthquake rupture parameters such as location, length, slip and magnitude (Hashash et al., 2015). In the historical archives, at least ten major earthquakes have been recorded since the 13th century (Chitrakar and Pandey, 1986).

2.4.1 Historical Earthquakes

The known major historical earthquakes in the region are listed below (Hashash et al., 2015, Chitrakar and Pandey, 1986). Many earthquake magnitudes can only be estimated because of lack of measurement values. M_L describes the magnitude on Richter scale and M_W the magnitude on moment magnitude scale.

- 1255 AD (June, 7): oldest known event, Kathmandu severely damaged, at least X on modified Mercalli scale (Rana et al., 2007), magnitude approximated around M_L 7.8, many collapsed houses and temples, one-third of population (including King) killed.
- 1260 AD: limited information available, collapse and severe damage of many buildings and temples, many casualties, following health epidemic and famine.
- 1408 AD: major earthquake, Rato Matchendranath temple completely destroyed, collapse and damage of many buildings and temples.
- 1505 AD: also known as Central Himalayan Earthquake, M_W 8.2, eventually two major earthquakes on 6 June and 6 July, collapse and severe damage of many buildings and temples, many casualties
- 1681 AD: limited information, many losses of lives, collapse and damage of many buildings and temples.
- 1767 AD: caused twenty-one aftershocks within twenty-four hours, no available information on loss of life or damage.
- 1810 AD: Twenty-one shocks within one month, small number of casualties, some buildings and temples destroyed or severely damaged.
- 1823 AD: seventeen shocks with moderate magnitudes, no documented casualties.

- 1833 AD: two main shocks (6 pm and 11 pm), most buildings, houses, public shelters and temples collapsed, Tower of Dharahara severely damaged, Thimi and Bakhatapur completely destroyed, 18,000 houses collapsed, 4,214 of them in Kathmandu Valley.
- 1834 AD: four major shocks during June and July, less strong than in 1833, excessive rain during the earthquake caused flooding of the Bagmati River, which damaged bridges.
- 1934 AD (January, 15): also known as Great Nepal Bihar Earthquake, highest number of casualties ever recorded, M_W = 8.1 (M_L = 8.4), 9.5 km south of Mount Everest, VII to X on Modified Mercalli scale over a widespread area, Mercalli Intensity X in Kathmandu Valley, most buildings destroyed in the three main cities of Kathmandu Valley, more than 8,500 people died, more than 126,000 houses severely damaged and more than 80,000 buildings completely collapsed. Especially in southern part of Kathmandu side effects modified ground motion strongly (Dixit et al. 1998). Sand and water vents appeared throughout the central vents of the earthquake area, surrounding ground subsided causing additional damage, also extensive liquefaction over a length of 300 m took place which caused many structures to go afloat.
- 1980 AD: M_L = 6.5, at far western portion of Nepal, 125 casualties, 248 seriously injured, 13,414 buildings severely damaged and 11,604 buildings completely destroyed.
- 1988 AD (August, 21): also known as Udaipur Earthquake, M_L = 6.9, eastern region, 721 deaths, 6,553 seriously injured, 65,000 damaged buildings.
- 1993 AD: M_L = 6.2, central and mid-western region, 1 death, 11 injuries, 451 damaged buildings, 72 collapsed houses.
- 1994 AD: M_L = 5.4, western region, 12 injuries, 84,000 buildings damaged, 623 collapsed houses.
- 1997 AD: central and far-west region, 1 reported injury, 60 buildings damaged, 196 houses collapsed.
- 2011 AD (September, 18): M_L = 6.9, widespread damage, intra-plate event in upper Eurasian or underlying Indian plate, 3 reported deaths, 164 injuries (30 critical), 6,000 houses collapsed, 14,000 houses damaged.

2.4.2 2015 M_W 7.8 Gorkha Earthquake

The 2015 Gorkha (Nepal) earthquake occurred on the 25 of April with a magnitude of M_W = 7.8 on or close to the MFT at a depth of ~15 km (Parameswaran et al., 2015; Galetzka et al. 2015, Lindsey et al. 2015). The rupture front in the subsurface extended from the eastern end of the great M_W 8.2 Central Himalayan Earthquake of 1505 to the western edge of the great M_W 8.1 Nepal Bihar earthquake of 1934 (Hashash et al., 2015). Bilham (1995) suggest a segmentation of the frontal fault in the boundaries of the rupture zone because it spans almost exactly between the 1505 and the 1934 earthquake rupture zones.

The main event occurred on or close to the MHT at an epicentral position of 18.1473 N and 84.7079 E and a hypocentral depth of 15 km. In the following two months, 260 aftershocks with > M_W 4.0 including 31 ≥ M_W 5.0 and 5 ≥ M_W 6.0 were recorded. The largest aftershock occurred on 12 May, 2015 with M_W 7.3, 140 km east of the main shock epicenter at an epicentral position of 27.809° N and 86.066° E (USGS ANSS catalog). In the first week after the main shock, 130 of them occurred, spanning through the entire rupture area (Fig. 5). Over the next couple of weeks, 17 aftershocks were recorded in the second week, 59 in the third and 54 in the following five weeks together.

Using finite-source models, Galetzka et al. (2015) calculated an average and peak slip of 0.69 and 6.67 m, with the peak occurring approximately north of the Kathmandu basin and a calculated duration of the major slip of 65 seconds.

Only one strong motion instrument (KATNP) at the U.S. embassy in the middle of Kathmandu basin recorded ground motion time-series over the bandwidth of engineering interest. The only rock outcrop ground shaking records are from continuous GPS stations run by the Caltech Tectonic Observatory, which could be used as a contribution to the strong motion records at KATNP (Hashash et al., 2015). Interesting about the records of KATNP are the very low peak ground acceleration (PGA) of 0.16 g and the very long period of 5 s of the predominant pulse, despite the large magnitude of M 7.8 and the very short epicentral distance. Also this earthquake has a very high ground slip magnitude (max. 6.5 m) and a very high peak ground velocity (80 cm/s, MMI IX) (Fig. 6) (Galetzka et al., 2015). Galetzka et al. (2015) explain these special features with source and side effects. There was a smooth onset of 6-7 s duration of the pulse because of the site of the earthquake near the brittle-ductile transition zone (Galetzka et al., 2015). This smooth onset excited a resonance of the Kathmandu basin, which produced violent shaking, with a period of 4 s and a protracted duration (Galetzka et al., 2015).

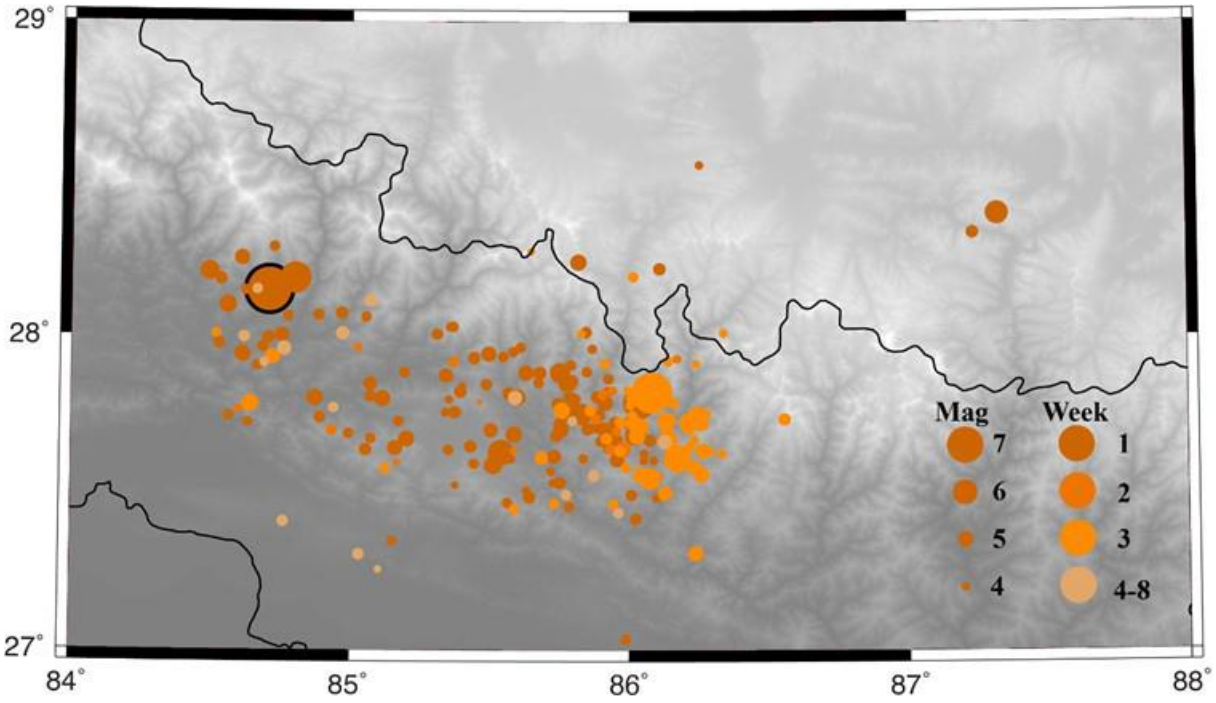

Fig. 5: Main shock (orange dot with black border) and related aftershocks > 4 M_W (orange dots) recorded in ANSS Catalog from 25 April and following two months (Hashash et al., 2015; modified after USGS ANSS catalog).

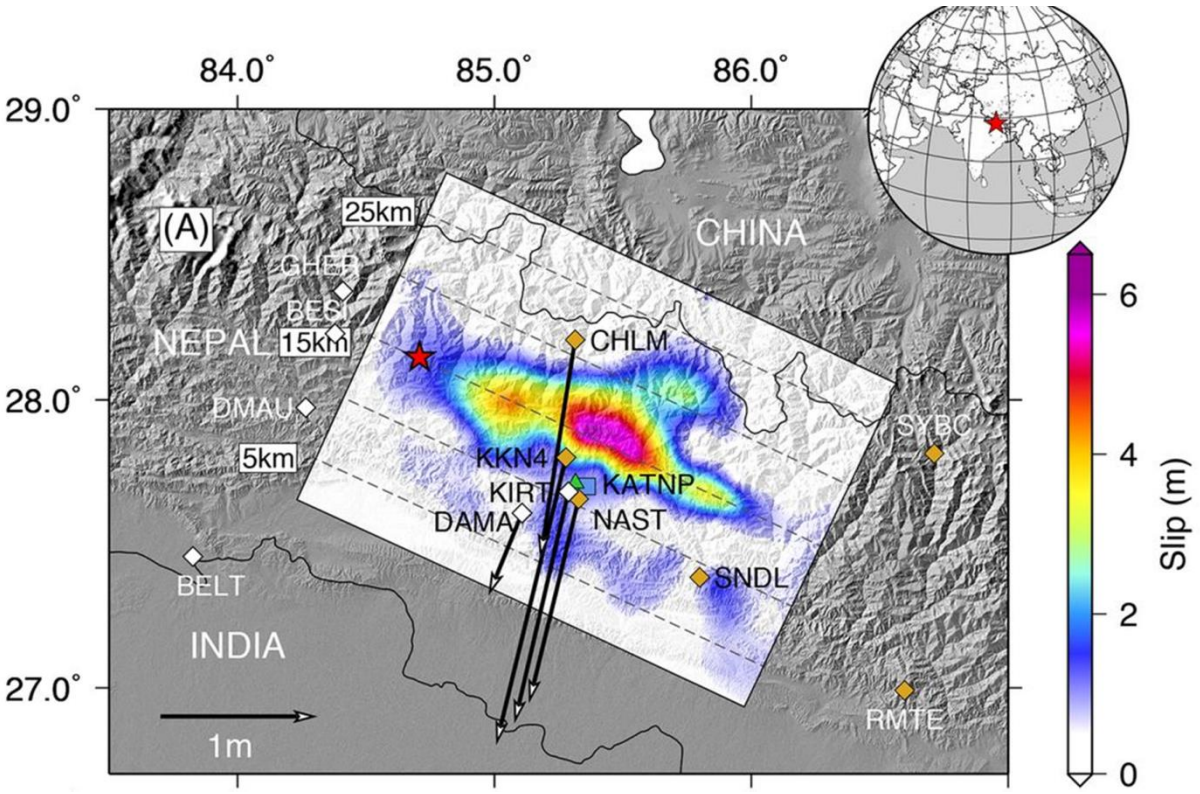

Fig. 6: Cumulative slip distribution due to the Gorkha earthquake. Slip inversion results for the Mw 7.8 Gorkha event. The red star marks the epicenter. Dashed contours are depths to the fault. Orange diamonds are 5 Hz cGPS stations and white diamonds are low rate (1/30 Hz) stations. The green triangle is the strong motion station. Kathmandu is represented by the blue square. The black arrows indicate the coseismic offsets measured at the sites. Vectors with less than 10 cm displacement are not shown (Galetzka et al., 2015).

2.5 Landslides

The mountainous topography of Nepal, with its steep slopes, has a high vulnerability for landsliding. Over the past 40 years, the average annual human death toll caused by landsliding has exceeded 110 lives per year (Nepal Ministry of Home Affairs, 2014). On top of this, approximately 100,000 households are damaged each year and the average annual property loss due to landslides counts USD 1,000,000 (Nepal Ministry of Home Affairs, 2014). As an example, the Jure Landslide on 5 August 2014 killed 168 people in a single slide and is not an exceptional case (Fig. 7) (Nepal Ministry of Home Affairs, 2014). Most landslides are triggered by the heavy rainfalls during the monsoon season, but some of them are also related to earthquakes (Tiwari and Marui, 1998). The 2015 Gorkha (Nepal) earthquake sequence, which includes the main shock and its related aftershocks triggered thousands of landslides, killing hundreds of people, blocking several roads, burying villages and damming rivers (Hashash et al., 2015). As this earthquake occurred in a relatively dry season (two months prior to the monsoon season), the extent of landsliding was significantly less than it could have been in conditions of fully saturated soil (Hashash et al. 2015). Nevertheless 8,330 landslides have been recorded in the three districts Rasuwa, Nuwakot and Dhading.

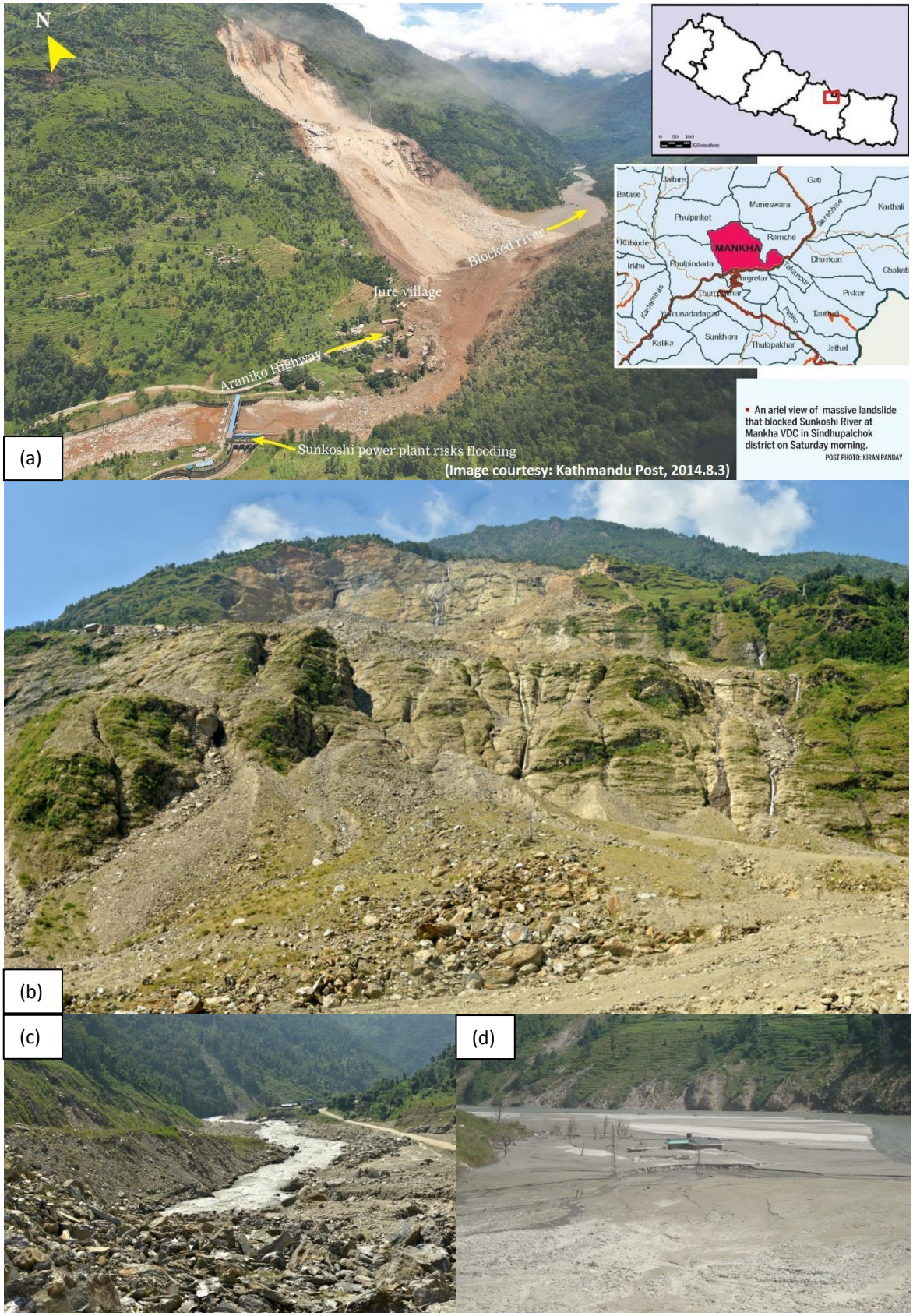

Fig. 7: Jure Landslide on the Araniko Highway occurred on 5 August 2014 killing 168 people (a) blocking Sunkoshi River and Araniko Highway (Kathmandu Post, 03.08.2014) (b) source area (http://www.gigapan.com/gigapans/180364) (c) view from deposit area downstream (http://www.gigapan.com/gigapans/180365) (d) view upstream showing houses with mud deposit settled in the reservoir generated by the blocking of the river by the landslide deposits.

3 Investigation Methods

Most of the work was done by remote sensing techniques. For this, many computer programs were used. The most important are Google Earth Pro, QGIS, Microsoft Excel and R Studio. First, the landslides were identified in Google Earth Pro. Then, landslide specific data was extracted within Google Earth Pro and QGIS. The data was stored, evaluated and analyzed in Excel and R Studio and maps (QGIS) and plots (Excel and R Studio) were generated. Additionally, field reconnaissance directly in Nepal was undertaken to evaluate the ground truthing.

3.1 Programs

The following programs were used for mapping the landslides and recording their data. Google Earth Pro was used for receiving the data of the position, surface area, aspect ratio, slope aspect, elevation of the bottom and the top of the slope and the evaluation of the effect on infrastructure (roads or villages). This data was collected, stored and evaluated in Microsoft Excel, including the calculation of the slope relief (top of slope – base of slope). The data was imported into QGIS and the slope angle, geologic unit, distance to the epicenter and the ground slip magnitude was evaluated for each landslide. For the slope angle, the global digital elevation model (GDEM) from the Shuttle Radar Topographic Mission (SRTM) was used. Then the data were analyzed by density and percentage plots, statistical relationship plots and maps (Excel and R Studio).

3.1.1 Google Earth Pro

For Nepal pre - and post - earthquake images are available with a resolution much higher than 15 m, but because their resolution is inconsistent, it is not possible to define an exact resolution for the whole research area. The images within our research area are from three corporations, namely DigitalGlobe, CNES / Astrium and NASA. The upgrade to Google Earth Pro was used because of its measuring areas and radius extension, which was used for measuring the surface areas of the studied landslides.

With Google Earth Pro the following data were analyzed for each landslide (Fig. 8):

- Earthquake (EQ) induced or pre – existing but reactivated
- Coordinates (yellow pins)
- Surface area (white lines)
- Aspect ratio
- Slope relief
- Slope aspect
- Affected infrastructure (roads or villages)

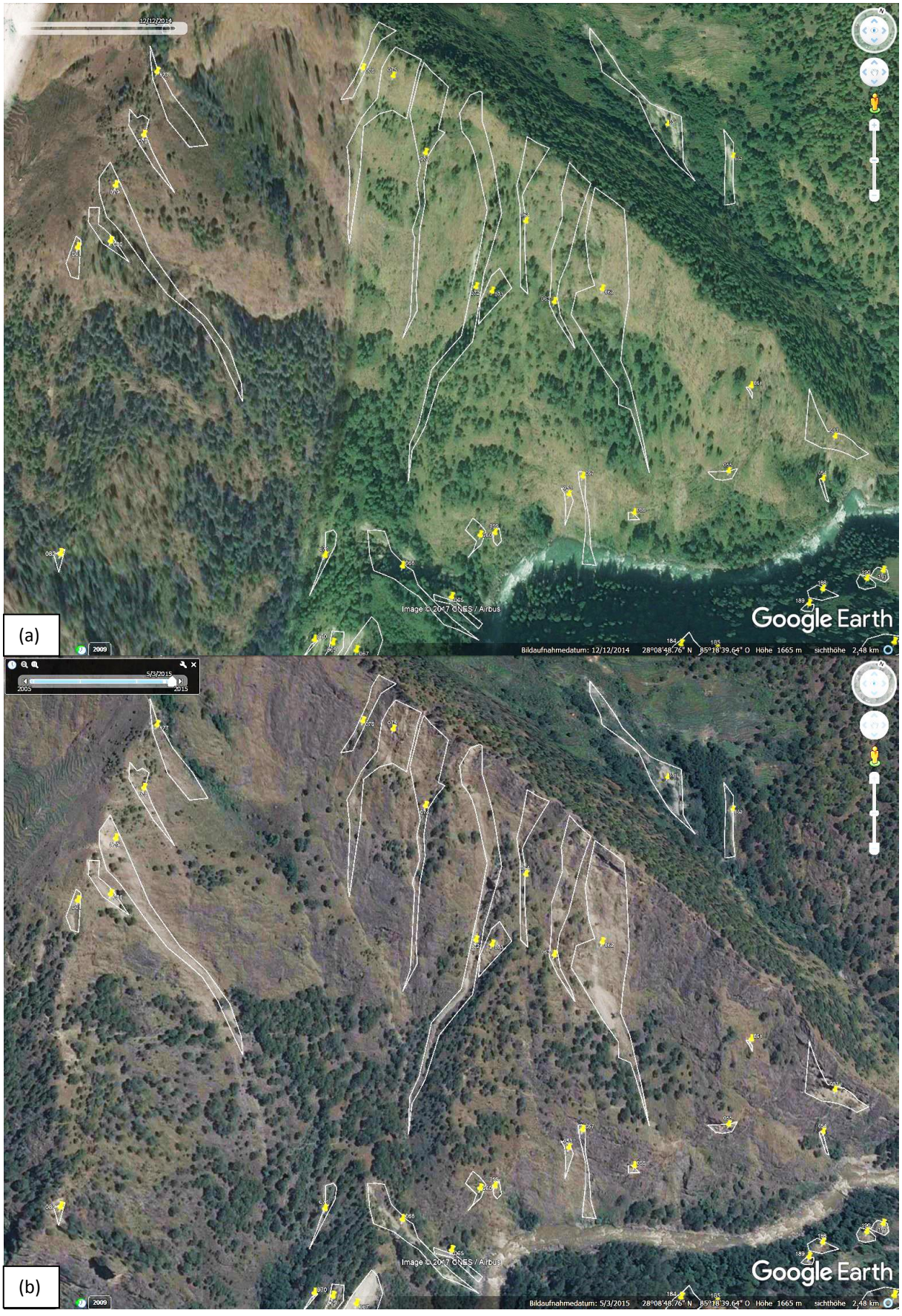

Fig. 8: Screenshot of Google Earth Pro with landslide marks (yellow pins) and polygons (white lines); (a) images taken before the earthquake (12.12.2014) (b) images taken after the earthquake (03.05.2015); special attention should be paid to the loss of vegetation; Image © 2016 Digital Globe and 2016 CNES / Astrium

3.1.2 QGIS

QGIS is an open-source and cross-platform free GIS program for data viewing, editing and analyzing. QGIS allows everyone to modify it for their purpose and therefore it has many additional functions like the open - source GIS integrations SAGA and GRASS. By using these two integrations many data could be extracted. Capabilities become also extended by plugins written in Python or C++ like the OpenLayers plugin which generates layers with open source virtual globe and virtual map programs like Google Earth or Bing Maps.

In QGIS the following data were analyzed:

- Geologic unit
- Distance from epicenter
- Elevation
- Ground slip magnitude

3.1.3 R Studio

R Studio is an integrated development environment for the statistical computing and graphics programming language R. R itself was developed by the R Core Team and appeared first in 1993. Within the last years, the popularity of the program increased essentially. R Studio and R itself are free of charge and open-source. In R the data crossplots were made.

3.2 GIS Data Representation and Analysis

The estimated parameters (surface area, slope angle, geological unit, etc.) which were determined for each individual landslide, were chosen because of their high influence on the landslide susceptibility or the population. In addition, in some cases the imagery could be used to distinguish between earthquake induced (Fig. 9 a, b) and pre – existing landslides. If a landslide was identified as pre – existing, it was evaluated whether it was reactivated by the earthquake (Fig. 9 c, d) or not reactivated (Fig.9 e, f). Only the earthquake induced and the reactivated, pre – existing landslides were considered. The following methods were used to estimate the values:

- The **surface area** of each landslide was measured in Google Earth Pro by putting a polygon on top of it, outlining the landslide and reading out the surface area of this polygon with the KML Manager program.
- The **slope angle** of the landslides was calculated in QGIS using the Global Digital Elevation Model from the Shuttle Radar Topographic Mission. With the digital elevation model analysis tool "Terrain Models", a slope steepness raster was generated. Based on this raster, the mean slope angle of each landslide was sampled with a plugin called "Point sampling tool".
- The **geology** of each landslide was determined based on the Geological Map of Nepal, 1994. The map was first digitized and then georeferenced within QGIS. The geology was hence divided into the groups indicated in the table:

na	**Nawakot Group**: Precambrian to Lower Paleozoic. Mainly **shallow marine sediments**; lower part dominantly clastic (phyllites, sandstones, quartzites and calcareous sandstones). Stromatolitic limestones and black slates occur in the upper part. Basic sills and dykes present.
kn	**Kuncha Group**: Precambrian. Mainly **flyschoid sequence** (bedded schists, phyllites and metasandstones), locally shallow water quartzite beds and basic sills and dykes present.
ph	**Phulchauki Group**: Early to Middle Paleozoic, fossiliferous (crinoids and trilobites) **calcareous rocks** with subordinate siliceous and argillaceous sediments in the upper part. Lower part: clastic and feebly metamorphosed rocks (phyillites, quartzites and siltstones).
Org	**Igneous Rocks**: Ordovician. Two **mica granites** with tourmaline.
kgn	**Igneous Rocks**: Precambrian and probably Paleozoic: **Augen gneisses** and two **mica granites** mainly in Kuncha Group, some also in Nawakot Group.
Qh	**Higher Himalaya**: Plio-Pleistocene to **Quaternary**. Mainly **fluvial and fluvio torrential sediments** with local lacustrine clays and marlstones.
hx	**Higher Himalayan Crystallines**: Precambrian high grade metamorphic rocks comprising **gneisses, quartzites and marbles**. Migmatites and granite gneisses present predominantly in the upper part.
Tgr	**Higher Himalayan Crystallines. Tertiary** (Miocene). Two **mica leucocratic granites** with tourmaline.

Tab. 1: Geological units from Geological Map of Nepal, 1994 © Department for Mines and Geology, Nepal (DMG)

- The **aspect ratio** was assigned by visual comparison of the ratio of the landslides in Google Earth Pro to a template. The values of aspect ratio were divided into eleven classes (1:1, 1:2, 1:3, 1:4, 1:5, 1:7, 1:10, 1:20, 1:50, 1:80 and 1:100).
- The **slope aspect** was assigned with the compass in Google Earth Pro and grouped in eight cardinal direction classes (N, NE, E, SE, S, SW, W, NW).

Fig. 9: Comparison of Google Earth images to estimate whether a landslide is pre – existing or earthquake induced; (a), (c) and (e) show images before earthquake, (b), (d) and (f) show images after earthquake; (a) and (b): earthquake induced landslide because no landslide is visible before the earthquake; (c) and (d): pre – existing but not reactivated landslide because the landslide looks exactly the same on both pictures; (e) and (f): pre – existing but reactivated landslides because a fan of the old landslide is visible but the appearance has changed significantly; Images © 2016 CNES / Astrium and 2016 Digital Globe.

- The **slope relief** gives the height of the slope from the base to the top on which the landslide occurred. Strong differences in the steepness divide the slope into several sub-slopes. Slope relief was calculated as H_T - H_B, where H_T is the elevation of the top and H_B is the elevation of the base of the slope. The values were singled out from Google Earth Pro.
- The **distance from the epicenter** was computed in Excel with the equation:

$$Radius_{Earth} * \arccos[\sin(lat_{LS}) * \sin(lat_E) + \cos(lat_{LS}) * \cos(lat_E) * \cos(lon_E - lon_{LS})] = D$$

  $Radius_{Earth}$ stands for the radius of the earth in kilometer, lat_{LS} for the latitude of the landslide in radiant, lat_E for the latitude of the epicenter in radiant, lon_{LS} for the longitude of the landslide in radiant, lon_E for the longitude of the epicenter in radiant and D for the distance in kilometer.
- The determination, if the considered landslides **affected infrastructure** (roads and villages) was evaluated by inspecting imagery in Google Earth Pro (Fig 10). The method was limited by the resolution of available imagery.
- The **elevation** is represented by a point within the landslide (Fig. 10). With the "Point Sampling Tool" in QGIS, the elevation of this point was extracted using the GDEM. Then the elevation was divided in 100 m classes, starting with an elevation from 200 to 300 m and ending with the class > 4800 m.
- The **landslide density** map was created with the "Heatmap" plugin in QGIS. By taking 564 m as radius, the landslide density within one square kilometer was evaluated. Besides, isolines were created with the "Contour" plugin in QGIS.
- For the estimation of the **ground slip magnitude,** the imagery published by Galetzka et al. (2015) was used.

Fig. 10: Google Earth image of landslides affecting a road; Image © 2016 CNES / Astrium.

3.3 Maps

The landslides are displayed in the maps are either shown as single marks or as densities. The highest observed landslide density was 91 LS/km². If not mentioned differently, the base map of the generated maps is a Google Earth image inserted by the OpenLayers plugin. The slope angle and the elevation map show a background with a transparent hill shade raster (transparency of 48 %) and a DEM colored according to the height difference. The map with the ground slip magnitude uses the inversion results from the paper published by Galetzka et al. (2015). The peak ground acceleration (PGA) map uses the PGA map from the Earthquake Damage Analysis Center (2015) as basemap. For the geological map, the Geological Map of Nepal, 1994 was overlaid by the landslide density.

3.4 Field reconnaissance

Two weeks of field reconnaissance were undertaken, to gain a better insight into the liability of the dataset, to perform a more detailed investigation on the landslides and their moving mechanisms, to examine the effects on the infrastructure and to investigate the effect of the monsoon on the landslides and the landslide conditions. During this field reconnaissance, the areas which were most influenced by landsliding and which were easily reachable were investigated. The investigated districts include Rasuwa (Trishuli Highway), Nuwakot, Dhading and Sindhupalchok (Araniko Highway, research area of Mirjam Ziselsberger, studying group colleague) (Fig. 11). Most of this field work was done by car, followed by detailed investigation by foot. Many landslides were (camera-) documented and some of them (mainly the ones affecting infrastructure) were investigated more closely. Specific areas were documented with the GigaPan Systems. These pictures can be interactively looked at by searching on the GigaPan website for TUGEnGeo (http://www.gigapan.com).

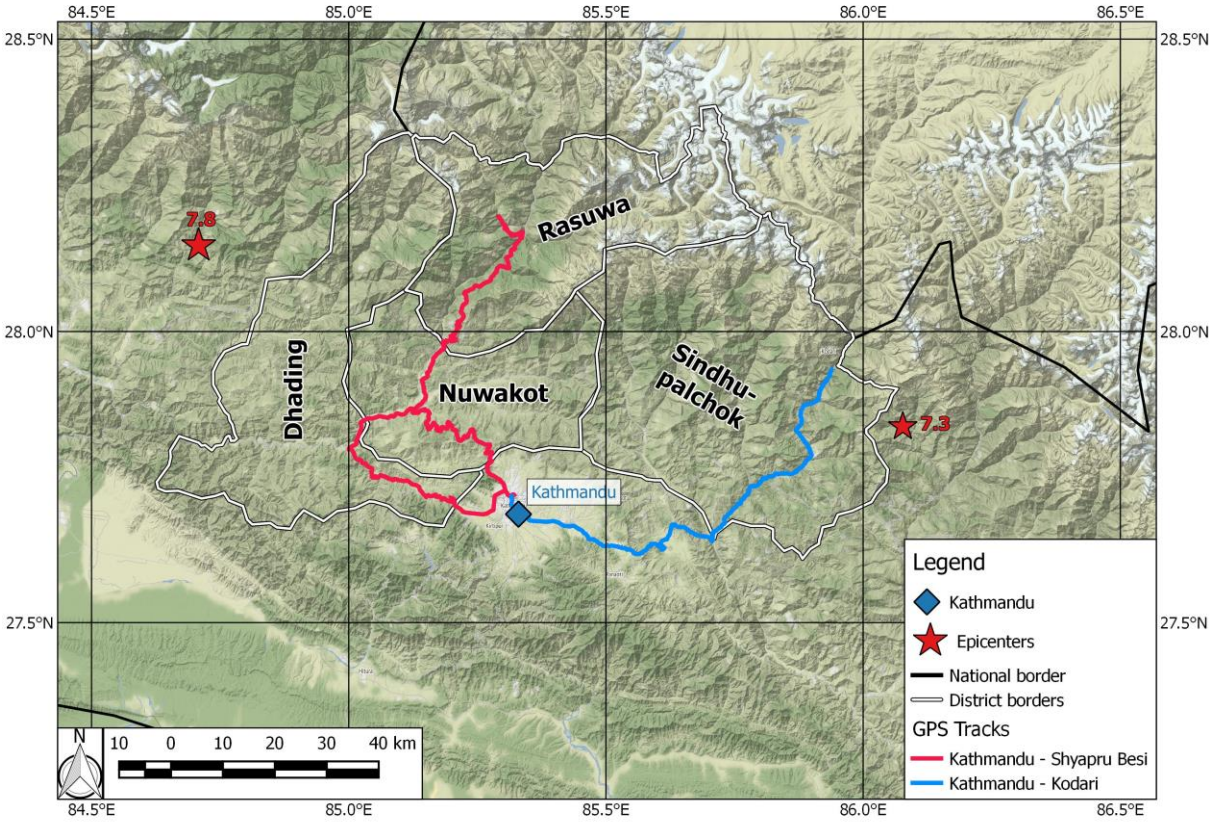

Fig. 11: Field reconnaissance routs. The investigated areas were Rasuwa (Trishuli Highway), Nuwakot, Dhading and Sindhupalchok (Araniko Highway, research area of Mirjam Ziselsberger, studying group colleague)

4 Data Analysis and Interpretation

The data analysis and interpretation of the investigations are divided into five chapters. The first chapter shows general statistics of the landslide data. The second chapter examines the relations between different landslide aspects. The third chapter focuses on correlation plots of four areas of intense landsliding. The forth chapter describes the maps and the general geographic tendencies of the landslide data and the fifth chapter is concerned with the field reconnaissance. The entire investigated area has a landslide density of 1.81 landslides per km². In Rasuwa a total number of 3175, in Dhading 3423 and in Nuwakot 1732 earthquake induced or pre – existing but reactivated landslides were detected.

4.1 Parameter Statistics

This chapter shows general statistics of the landslides with histograms, bar plots or spider diagrams. In addition to these figures, another one was added to show the percentage of earthquake induced and pre – existing but reactivated landslides (Fig. 12). In the entire research area, 86 % of the landslides were earthquake induced and 14 % were pre – existing but reactivated. This means that the majority of landslides was earthquake induced and only a minor amount of them was pre - existing but reactivated. The reason for this trend is most likely due to the difficulty to identify a pre – existing landslide with the used imagery and therefore many landslides classified as earthquake induced may actually be pre – existing but reactivated ones.

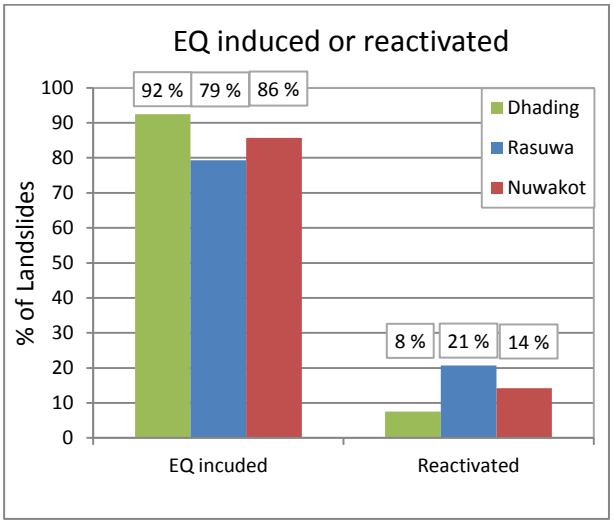

Fig. 12: Barplot which shows whether landslides are earthquake induced or pre – existing but reactivated.

- **Surface area:** Fig. 13 displays the distribution of the surface area classes (100 m²) of the landslides as commonly performed in landslide statistics on a logarithmic scale (base of 10) (e.g. Xu et al. 2014a). The plot shows that most of the landslides have a small surface area, with its peak at 200 m² (almost 50% of the landslides have a surface area smaller than 1000 m²). The resolution threshold is at approximately 200 m² and after this peak, the number decreases exponentially to the biggest landslide, the Langtang mass movement, with a surface area of 1.28 km². 24 landslides bigger than 100,000 m² are not displayed in the diagram because of reasons of illustration. In earthquake triggered landslide inventories, the trend of a decreasing number of landslides with increasing surface area is well known and similar to other publications (Guzzetti et al., 2002; Malamud et al., 2004; Xu et. al., 2014a).

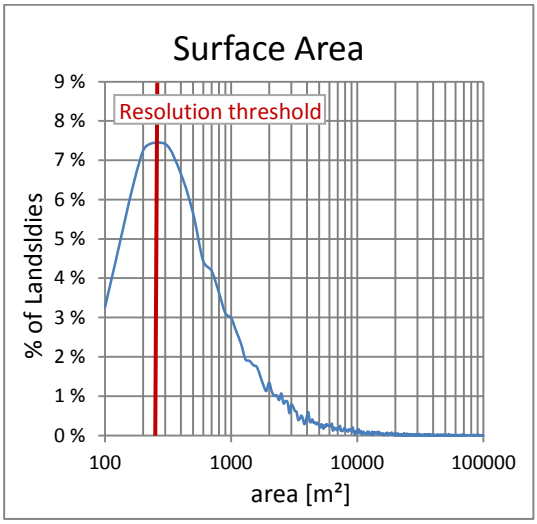

Fig. 13: Distribution of surface area classes histogram (blue, 100 m² classes, x – axis logarithmic to the base of 10), resolution threshold (red) at approximately 200 m².

- **Slope angle:** In Fig. 14, the blue bars show the area distribution of slope angle classes over the whole research area. The red bars show the number of landslides which occurred in each of these classes divided by the area of this class. The value of the area bars is given in square kilometers (km²); the value of the density bars is given in landslides per square kilometer (LS/km²). The distribution of the total area is close to a normal distribution with its peak between 25° - 30°, showing that most of the slopes in the research area have a slope angle between 25° - 30°. The distribution of the landslide density is shifted to the steeper angles and has its peak of 4.45 LS/km² at 50° - 55°. This plot indicates that the slope angle has a high influence on the landslide occurrence and that landslides are much more likely to occur on steeper slopes.

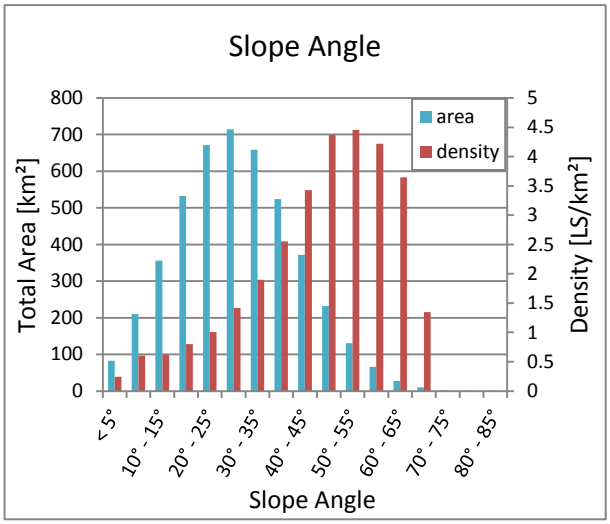

Fig. 14: Slope angle distribution barplot, blue bars indicate the area distribution of slope angle classes over the whole research area. The red bars indicate the number of landslides which occurred in each of these classes divided by the area of this class. The value of the area is given in square kilometers (km²), the value of the density is given in landslides per square kilometer (LS/km²).

- **Geology:** In Fig. 15, the blue bars show the area distribution of geological formations over the whole research area. The red bars show the number of landslides which occurred in each of these formations divided by the area of this class. The value of the area bars is given in square kilometers (km²), the value of the density bars is given in landslides per square kilometer (LS/km²). Fig. 15 displays that the Augen gneisses and mica granites of the Kuncha Group and Nawakot Group (kgn) have the highest landslide density (11 LS/km²). The second highest density, which is much smaller, occurred in the Kuncha Group (3.3 LS/km²). It can be concluded that these two formations have a much higher susceptibility for landsliding than the others. This fact may be due to structural, textural and weathering properties.

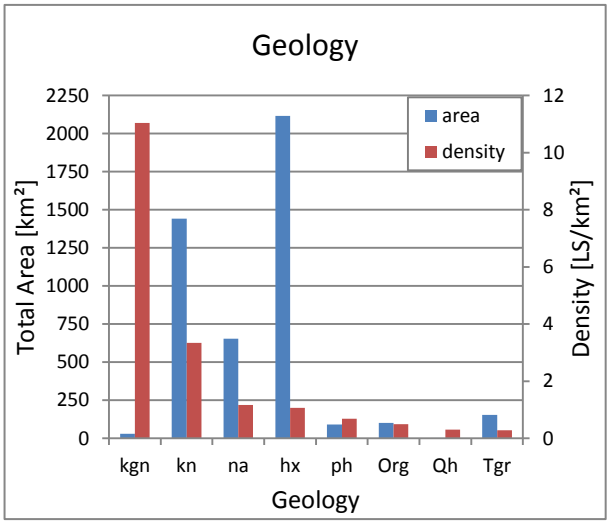

Fig. 15: Geological formation barplot, blue bars indicate the area distribution of the geological formations over the entire research area. The red bars indicate the number of landslides which occurred in each of these formations divided by the area of this class. The value of the area is given in square kilometers (km²), the value of the density is given in landslides per square kilometer (LS/km²).

- **Aspect ratio:** Fig. 16 displays the percentage of each aspect ratio class in relation to the total number of landslides. The plot shows that landslides with an aspect ratio of 1:10 are the most common ones and that the biggest amount of landslides has an aspect ratio between 1:1 and 1:10. This figure also shows a general trend that almost no narrow and/or very long landslides were triggered.

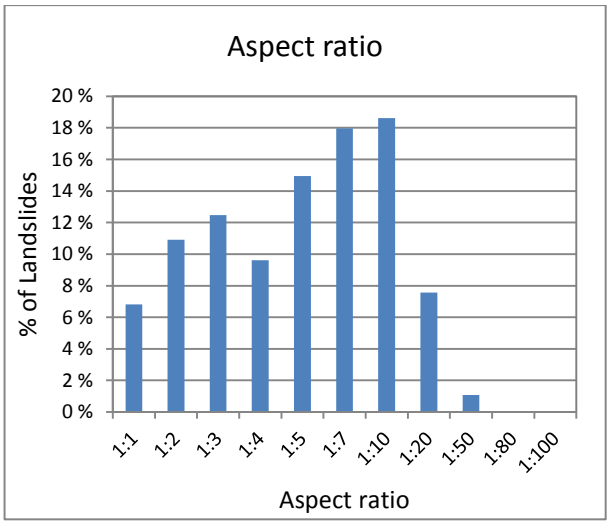

Fig. 16: Aspect ratio barplot, showing percentage of each class in relation to the total number of landslides.

- **Slope aspect:** Fig. 17 shows a spider diagram, where the blue line shows the area distribution of the slope aspect classes over the entire research area. The red line shows the number of landslides which occurred in each of these classes divided by the area of this class. The value of the area is given in square kilometers (km²), the value of the density is given in landslides per square kilometer (LS/km²). The red line shows a strong increase of the landslide density in southern and western direction whereas the blue line shows that the area distribution of each slope aspect class is almost the same for the entire research area. This indicates that there was a much higher tendency for landslides to occur in southern and western direction. Several authors have described strong effects of the slope aspect on the landslide susceptibility (Guzzetti et al., 1999; Evans et al., 1999, Nagarajan et al., 2000; Yalcin, 2008). These authors have identified general trends which could increase the landslide susceptibility even before an earthquake occurs by affecting the vegetation, the weathering, the degree of saturation and the rock mass strength. These factors include exposure to sunlight, drying winds, rainfall and discontinuities. The direction of the ground slip, which was in this case to the south, can have an influence too.

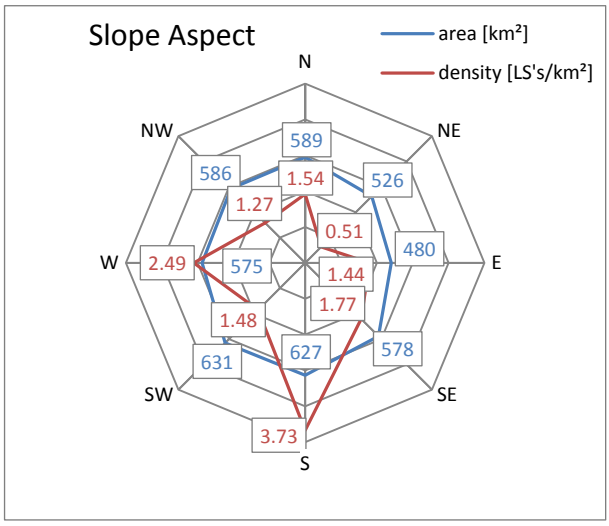

Fig. 17: Slope aspect spider diagram, where the blue line indicates the area distribution of slope aspect classes over the entire research area. The red line indicates the number of landslides which occurred in each of these classes divided by the area of each class. The value of the area is given in square kilometers (km²), the value of the density is given in landslides per square kilometer (LS/km²).

- **Slope relief:** Fig. 18 displays the percentage of the number of each slope relief class in relation to the total number of landslides. It shows that most of the landslides occurred on slopes with a slope relief between 120 and 180 m. Before this peak, the frequency rises almost linearly and afterward, it decreases exponentially to the maximal measured slope relief of 2372 m. The main reason why most landslides happened on slopes with small slope reliefs is the much higher presence of slopes with small slope reliefs. Another factor is that the high ground slip magnitudes, which increases the landslide susceptibility significantly, are in the southern part of the research area where small slope reliefs are present.

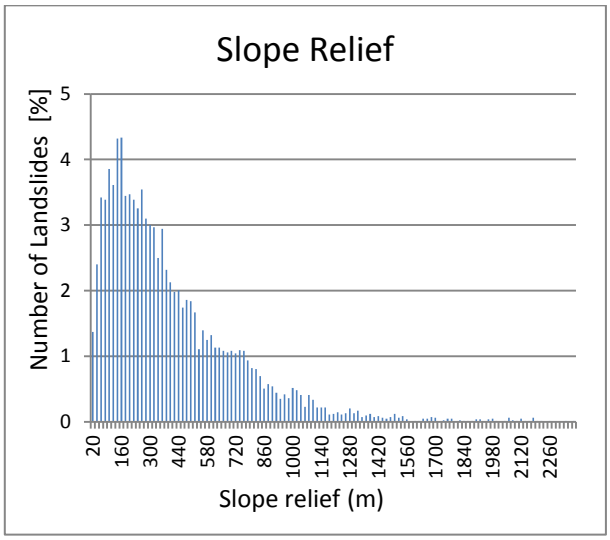

Fig. 18: Distribution of slope relief classes histogram (20 m classes).

- **Distance to the epicenter:** In Fig. 19, the blue bars indicate the area distribution of the distance (from the epicenter) classes over the whole research area. The red bars indicate the number of landslides which occurred in each of these classes divided by the area of this class. The value of the area bars is given in square kilometers (km²), the value of the density bars is given in landslides per square kilometer (LS/km²). The area bars illustrate an overall normally distributed area with its peak at 45 - 50 km distance to the epicenter. The density on the other hand has its highest peak of 3.5 LS/km² at 25 – 30 km distance from the epicenter and also shows a very high density at a distance of 30 – 35 km. Before this peak the density increases strongly and after it the density decreases smoothly until reaching a value of zero at 85 – 90 km distance. It is obvious that the landslide density decreases with increasing distance from the epicenter. It is, however unobvious that the density does not have the highest values directly at the epicenter. This is possibly due to the low ground slip magnitudes close to the epicenter.

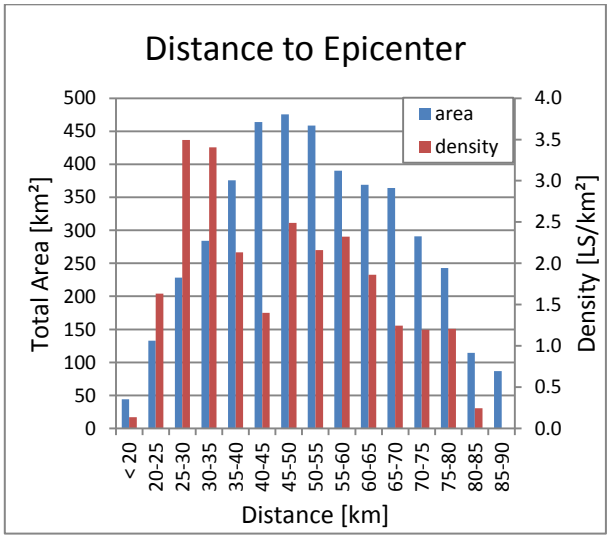

Fig. 19: Distance to epicenter barplot, blue bars indicate the area distribution of the distance classes over the whole research area. The red bars indicate the number of landslides which occurred in each of these classes divided by the area of this class. The value of the area is given in square kilometers (km²), the value of the density is given in landslides per square kilometer (LS/km²).

- **Affected Infrastructure:** Fig. 20 displays the number of affected infrastructure, namely roads and villages, for each district separately. In total, 1034 roads were hit by landslides and 25 villages were affected. By far the highest number of both categories was observed in Rasuwa with 443 landslides affecting roads and 19 landslides affecting villages. The lowest number of affected villages was in Nuwakot, namely only one, however, on the other hand, 319 landslides interfering with roads were identified. The lowest number of affected roads was in Dhading (272), but nevertheless five villages were hit by landslides. These statistic results indicate that almost every eighth landslide affected a road but only every 333 landslide affected a village. Nuwakot has the highest number of affected roads, whereas the number of landslides there is almost half of the number of Rasuwa or Dhading. This may be because of the much higher presence of infrastructure in Nuwakot in difference to the other two districts. The high number of affected infrastructure in Rasuwa can be correlated to the area of the highest landslide density, namely southwestern Rasuwa.

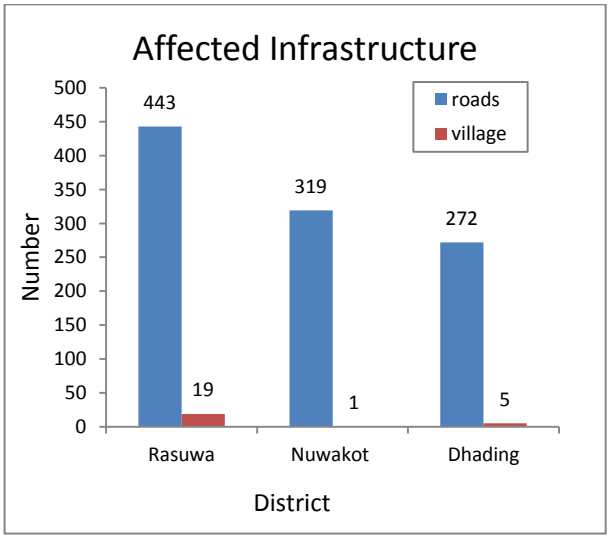

Fig. 20: Affected infrastructure barplot, blue bars indicate affected roads, red bars indicate affected villages, values given in total numbers.

- **Elevation:** In Fig. 21, the blue bars indicate the area distribution of the elevation classes over the entire research area. The red bars indicate the number of landslides which occurred in each of these classes divided by the area of this class. The value of the area bars is given in square kilometers (km²), the value of the density bars is given in landslides per square kilometer (LS/km²). This figure shows two important aspects. First, the main part of the research area is at lower elevations within the range of 500 to 1800 m a.s.l.. Second, the landslide density shifts to the right, so to higher elevations, and therefore the elevation has an influence on the landslide susceptibility (peak of 3.7 LS/km² between 1600 to 1700 m a.s.l.). The most likely reasons for this shift are the higher presence of steep slopes at higher elevations.

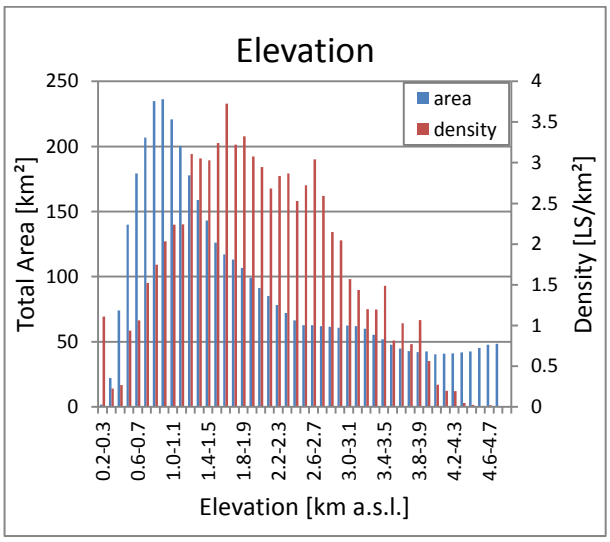

Fig. 21: Elevation barplot, blue bars indicate the area distribution of the elevation classes over the whole research area. The red bars indicate the number of landslides which occurred in each of these classes divided by the area of this class. The value of the area is given in square kilometers (km²), the value of the density is given in landslides per square kilometer (LS/km²).

- **Ground slip magnitude:** In Fig. 22, the blue bars indicate the area distribution of the ground slip magnitude classes over the entire research area (Galetzka et al., 2015). The red bars indicate the number of landslides which occurred in each of these classes divided by the area of this class (Galetzka et al., 2015). The value of the area bars is given in square kilometers (km²), the value of the density bars is given in landslides per square kilometer (LS/km²). Fig. 22 shows a distinct influence of the ground slip magnitude on the number of landslides which occurred. It displays that there is by far the highest landslide density at a magnitude between 3 to 5 m. The fact that the more the ground moves, the more landslides occur, is straight forward. The fact that the density decreases again at higher magnitudes can be related to the flat topography in the area, where the highest magnitudes occurred.

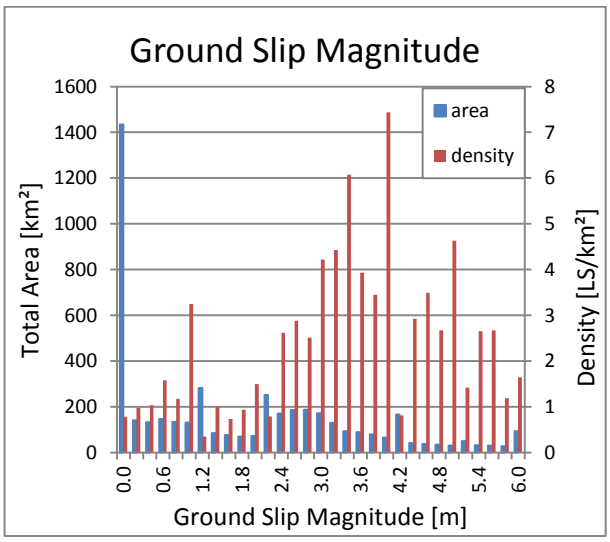

Fig. 22: Ground slip magnitude barplot, blue bars indicate the area distribution of the magnitude classes over the entire research area. The red bars indicate the number of landslides which occurred in each of these classes divided by the area of this class. The value of the area is given in square kilometers (km²), the value of the density is given in landslides per square kilometer (LS/km²).

4.2 Parameter Inter - Relationships

It is a well-known fact that landslide aspects have influence on one another, for example if a landslide happens on a slope with a high slope relief, it may have a bigger area because the landslide can travel further as it is not stopped by the valley bottom. For this reason, a few parameters were selected based on a correlation matrix and personal judgement, to be specifically examined concerning their correlation between each other. All these plots were done in R Studio. For all these plots, the biggest landslide, the Langtang mass movement, was not taken into account, as it represents a too massive outlier. For the smooth plots, the method gam (generalized additive models with integrated smoothness estimation line) was used.

- **Surface area vs. slope relief:** Fig. 23 crossplots the surface area with the slope relief as a jitter and a smooth plot. The surface area axis is logarithmic to the base of 10. This figure indicates a positive correlation between the slope relief and the surface area. Because the distance of the valley bottom is statistically further at higher slope reliefs, the landslides can travel longer distances which increases the surface area.

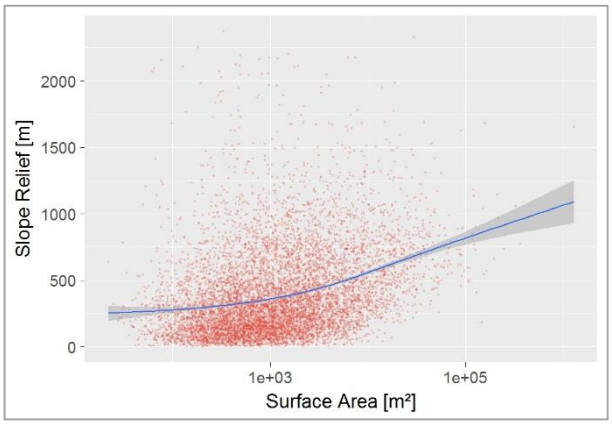

Fig. 23: Surface area vs. slope relief jitter and smooth plot, surface area axis logarithmic (base of ten).

- **Surface area vs. slope angle:** Fig. 24 crossplots the surface area with the slope angle as a jitter and a smooth plot. The surface area axis is logarithmic to the base of 10. The majority of landslides, namely those with a surface area between 200 and 2000 m, have a distinct positive correlation between the slope angle and the surface area. Thus, the higher the slope angles, the bigger the difference between the friction angle of the landslide material and the slope angle. The resulting driving force increases the displacement of the material and a bigger surface area evolves.

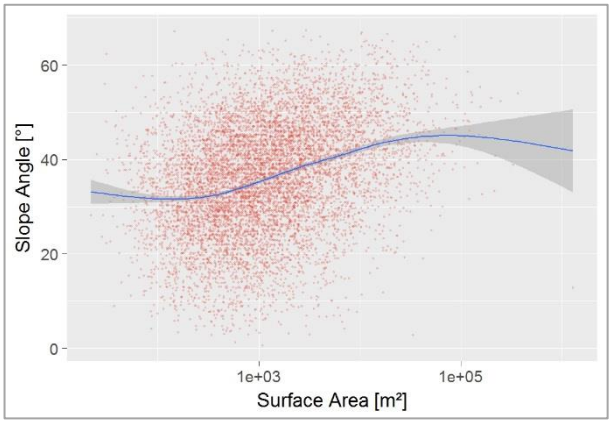

Fig. 24: Surface area vs. slope angle jitter and smooth plot, surface area axis logarithmic (base of ten).

- **Surface area vs. elevation:** Fig. 25 crossplots the surface area with the elevation as a jitter and a smooth plot. The surface area axis is logarithmic to the base of 10. The majority of landslides, namely those with a surface area between 200 and 2000 m, have a distinct positive correlation between the elevation and the surface area. This trend is due to the increase of the slope relief and the slope angle at higher elevations.

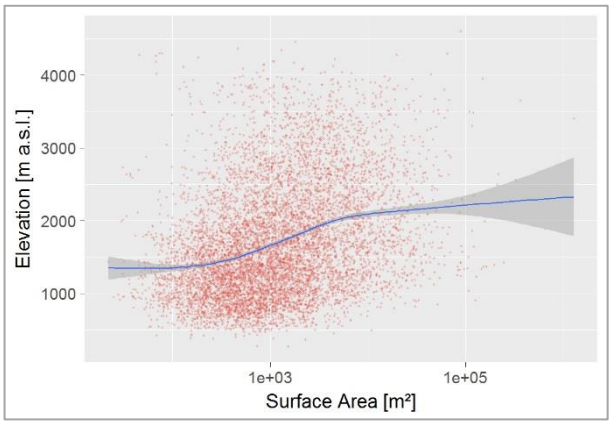

Fig. 25: Surface area vs. elevation jitter and smooth plot, surface area axis logarithmic (base of ten).

- **Surface area vs. aspect ratio:** Fig. 26 shows boxplots of the aspect ratio with respect to the surface area. The surface area axis is logarithmic to the base of 10. This figure indicates a positive correlation between the aspect ratio and the surface area. This means that the longer and narrower the landslides become, the bigger they grow. Because of the resolution of the imagery, only landslides broader than a certain amount could be detected. Therefore some small narrow landslides may not have been detected. Also, bigger landslides occur on slopes with higher slope relief which increases their length.

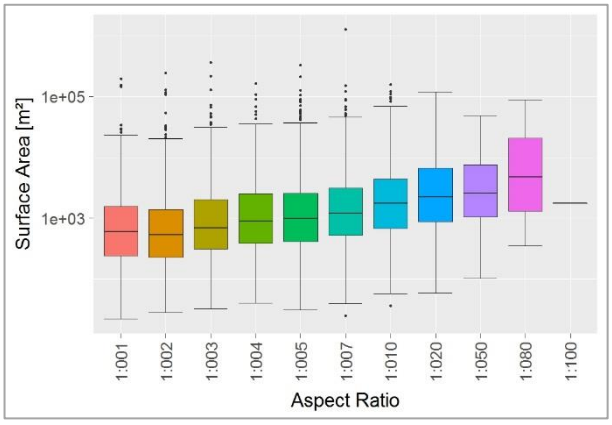

Fig. 26: Surface area vs. aspect ratio boxplot, surface area axis logarithmic (base of ten).

- **Surface area vs. geology:** Fig. 27 shows boxplots of the geology with respect to the surface area. The surface area axis is logarithmic to the base of 10. This figure indicates no certain trend except that in general the landslides occurring in the Tgr formation are much bigger than in the other ones. The Tgr formation is situated in the northeastern part of Rasuwa where a high elevation with steep slopes and high slope reliefs is present. The explanation for this high value is due to the geographical position, which is favorable for larger landslides.

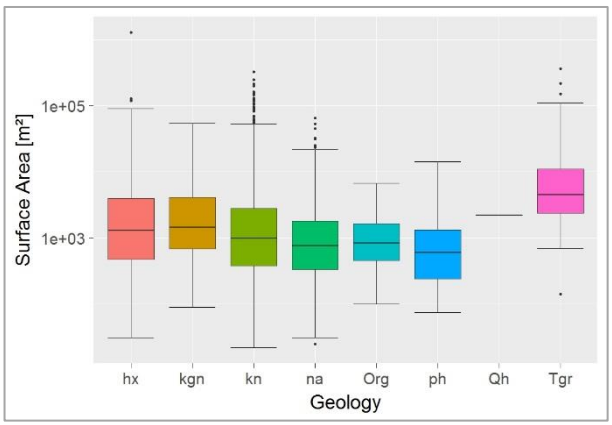

Fig. 27: Surface area vs. geology boxplot, surface area axis logarithmic (base of ten).

- **Surface area vs. ground slip magnitude:** Fig. 28 crossplots the surface area with the ground slip magnitude as a jitter and a smooth plot. The surface area axis is logarithmic to the base of 10. This figure indicates a negative correlation between the ground slip magnitude and the surface area. This means that the bigger landslide occurred in areas of lower ground slip magnitudes. This trend can be correlated with the high ground slip magnitudes found in areas of low elevation with low slope reliefs and flatter slope angles, whereas the area of high magnitude was in locations of little topography.

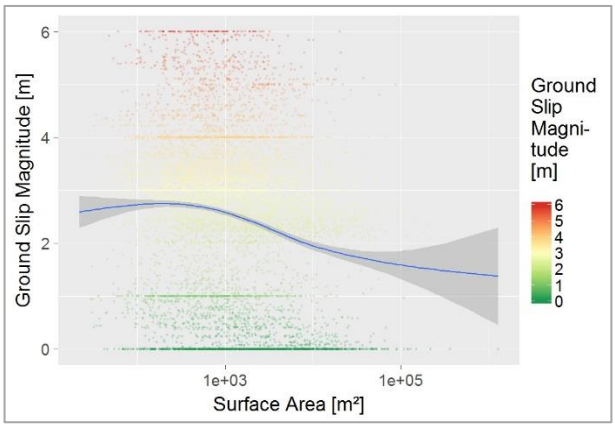

Fig. 28: Surface area vs. ground slip magnitude jitter and smooth plot, surface area axis logarithmic (base of ten).

- **Affected infrastructure vs. slope angle:** Fig. 29 shows boxplots of the affected infrastructure with respect to the slope angle, where no distinct trend is visible. This means that the affected infrastructure was not particularly located in steeper or flatter slopes.

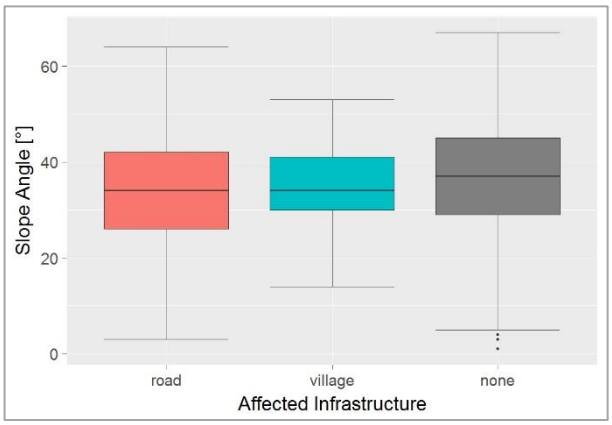

Fig. 29: Affected infrastructure vs. slope angle boxplot.

- **Affected infrastructure vs. elevation:** Fig. 30 shows boxplots of the affected infrastructure with respect to the elevation. This figure indicates that the mean value of the affected infrastructure was at lower elevations than the median of the landslides not affecting any infrastructure. As more inhabited areas are in lower elevations, this trend is obvious.

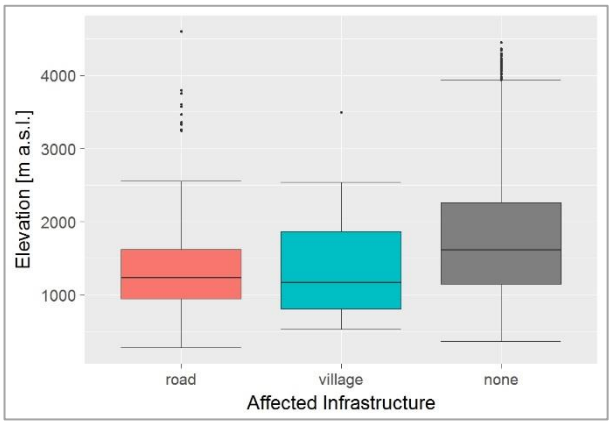

Fig. 30: Affected infrastructure vs. elevation boxplot.

- **Affected infrastructure vs. earthquake induced or pre – existing but reactivated landslides:** Fig. 31 shows barplots of the affected infrastructure with respect to the nature of the landslide, whether it was earthquake induced or pre – existing but reactivated. The values are stacked on top of each other with a normalized height. This figure indicates that reactivated landslides affected infrastructure more often than earthquake induced ones did. This trend is visible for both, roads and villages. The reason for this trend is not clear and needs further studying.

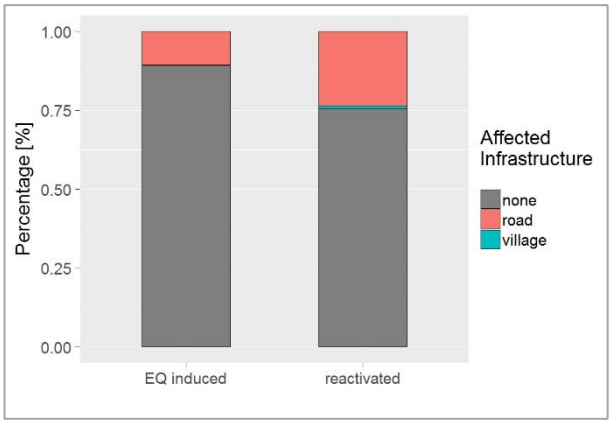

Fig. 31: Affected infrastructure vs. nature of landslide (earthquake induced (EQ induced) or pre – existing but reactivated (reactivated)) barplot, values are stacked on top of each other with a normalized height.

- **Aspect ratio vs. slope angle:** Fig. 32 shows boxplots of the aspect ratio with respect to the slope angle. This figure indicates a distinct positive correlation between the aspect ratio and the slope angle. This implies that at steeper slope angles, the landslides become longer and narrower. The increase of the displacement of the landslide material at steeper slopes explains this trend.

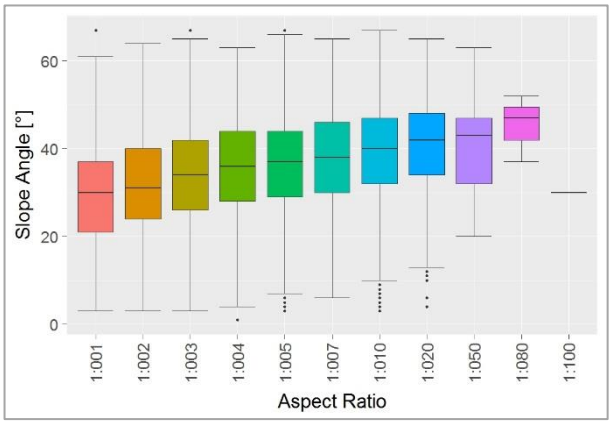

Fig. 32: Aspect ratio vs. slope angle boxplot.

- **Aspect ratio vs. slope relief:** Fig. 33 shows boxplots of the aspect ratio with respect to the slope relief. The slope relief axis is logarithmic to the base of 10. This figure displays a strong positive correlation between the aspect ratio and the slope relief. This indicates that at high slope reliefs, the landslides become longer and narrower. The increase of the displacement of the landslide material at higher slope reliefs explains this trend.

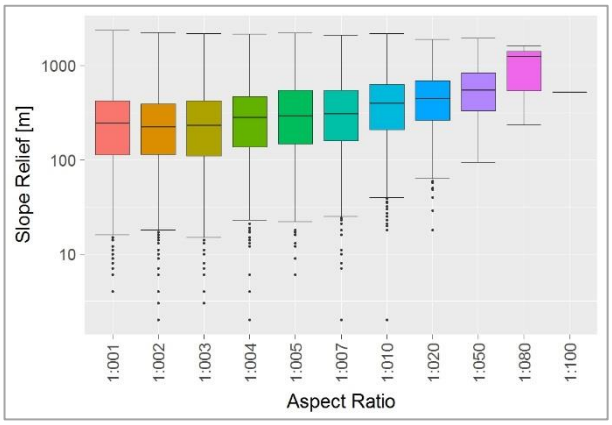

Fig. 33: Aspect ratio vs. slope relief boxplot, slope relief axis logarithmic (base of ten).

- **Aspect ratio vs. ground slip magnitude:** Fig. 34 shows boxplots of the aspect ratio with respect to the ground slip magnitude and displays a negative correlation between the aspect ratio and the magnitude. This indicates that at lower magnitudes, the landslides become longer and narrower. At areas with little topography, the slope relief sand the slope angles are low. As these parameters affect the aspect ratio strongly and as the highest values of the ground slip magnitude were in areas with little topography, the decrease of the aspect ratio at higher ground slip magnitudes can be explained.

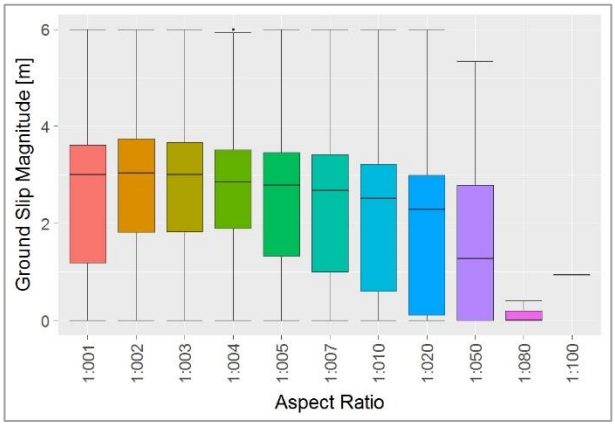

Fig. 34: Aspect ratio vs. ground slip magnitude boxplot.

- **Aspect ratio vs. elevation**: Fig. 35 shows boxplots of the aspect ratio with respect to the elevation and reveals a positive correlation between the aspect ratio and the elevation. This indicates that at lower elevations, the landslides became broader and shorter. At low elevation areas, the slope relief and the slope angle are low. As these parameters affect the aspect ratio strongly, the decrease of the aspect ratio at low elevations can be explained.

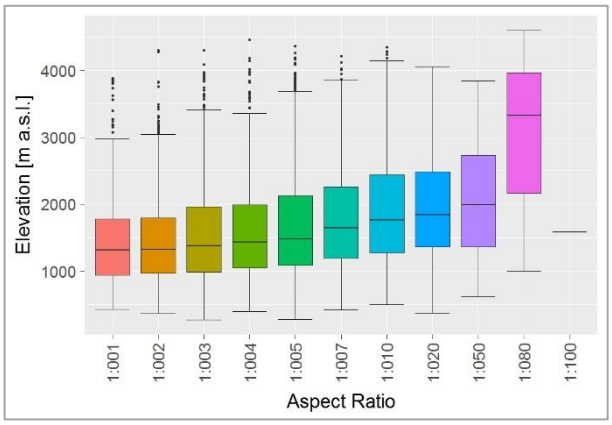

Fig. 35: Aspect ratio vs. elevation boxplot.

- **Slope aspect vs. aspect ratio:** Fig. 36 shows barplots of the slope aspect with respect to the aspect ratio. The values are stacked on top of each other with a normalized height. In this figure, no real correlation can be seen. This means that the aspect ratio of the landslides is not related to the slope aspect.

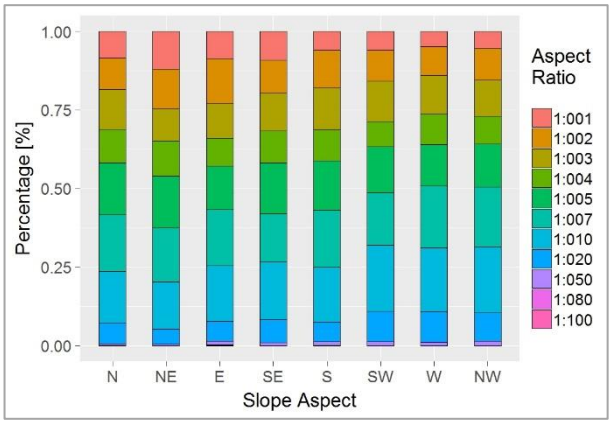

Fig. 36: Aspect ratio vs. slope aspect boxplot.

- **Slope angle vs. elevation:** Fig. 37 crossplots the slope angle with the elevation as a jitter and a smooth plot. This figure indicates a positive correlation between the slope angle and the elevation. At higher elevations, the topography generally increases, also increasing the amount of steep slopes. This plot confirms the tendency of an increasing slope angle with increasing elevation.

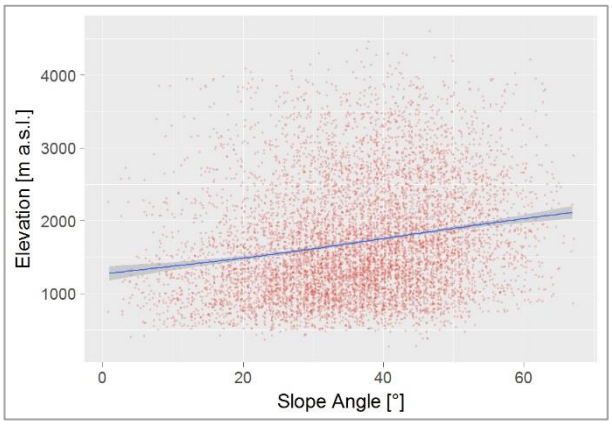

Fig. 37: Slope angle vs. elevation jitter and smooth plot.

- **Slope relief vs. elevation:** Fig. 38 crossplots the slope relief with the elevation as a jitter and a smooth plot. Approximately 70% of all the landslides happened at an elevation lower than 2000 m a.s.l.. Within this part, the elevation and the slope relief have a positive correlation. This figure confirms the assumed correlation between the elevation and the slope relief. It also shows that this correlation is only correct until a certain point, which is approximately at 2000 m a.s.l.. After this peak no distinct correlation is visible.

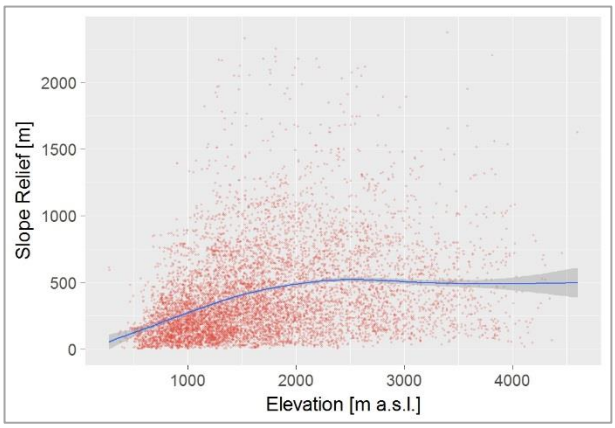

Fig. 38: Slope relief vs. elevation jitter and smooth plot.

- **Slope relief vs. slope angle:** Fig. 39 crossplots the slope relief with the slope angle as a jitter and a smooth plot and indicates a positive correlation between the slope relief and the slope angle. This means that if the slope relief increases, statistically the slope angle increases too. This correlation is due to the fact that both of these values increase with increasing elevation.

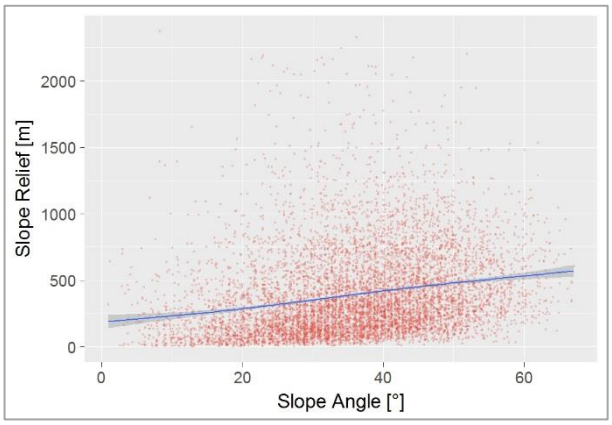

Fig. 39: Slope angle vs. slope relief jitter and smooth plot.

- **Geology vs. slope angle:** Fig. 40 shows boxplots of the geology with respect to the slope angle. In this figure no distinct trend is visible. The major output of these plots is that the high landslide density in the geological formations kgn and kn cannot be related to higher slope angles in these formations.

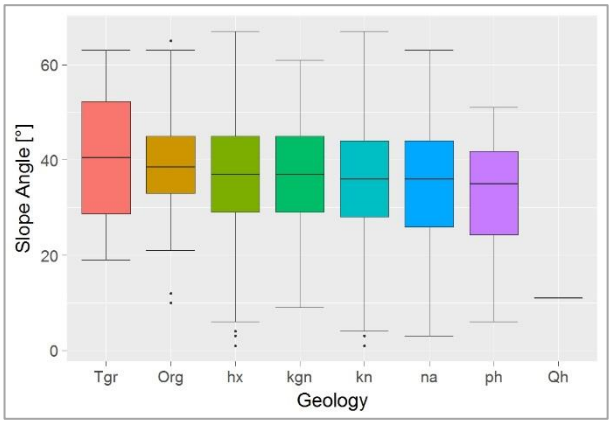

Fig. 40: Geology vs. slope angle boxplot.

- **Slope aspect vs. slope angle:** Fig. 41 shows boxplots of the slope aspect with respect to the slope angle. In this figure no distinct trend is visible. The major output of these plots is that there is no tendency to steeper southern or western slopes. Therefore the higher landslide density on southern and western slopes cannot be correlated to a slope angle trend at these slope orientations.

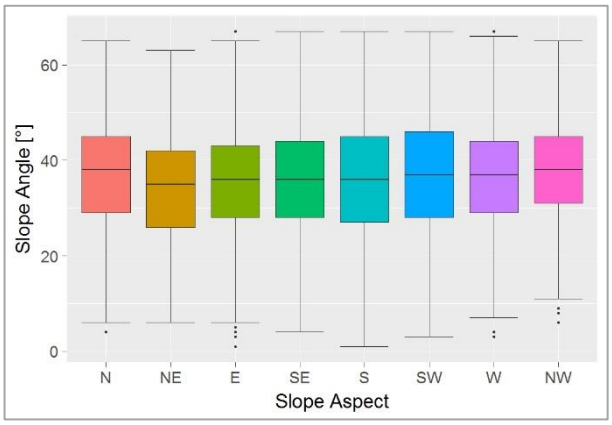

Fig. 41: Slope aspect vs. slope angle boxplot.

4.3 Areas of intense landsliding

For a more detailed evaluation, four geographical areas were selected based on their high landslide density (Fig. 42). The number of landslides within each area of intense landsliding (AIL) counts 83 for area 1, 66 for area 2, 308 for area 3 and 888 for area 4. The datasets of each area were analyzed, evaluated and compared. The parameters chosen to be compared and displayed were the slope angle, the slope aspect, the elevation and the geology.

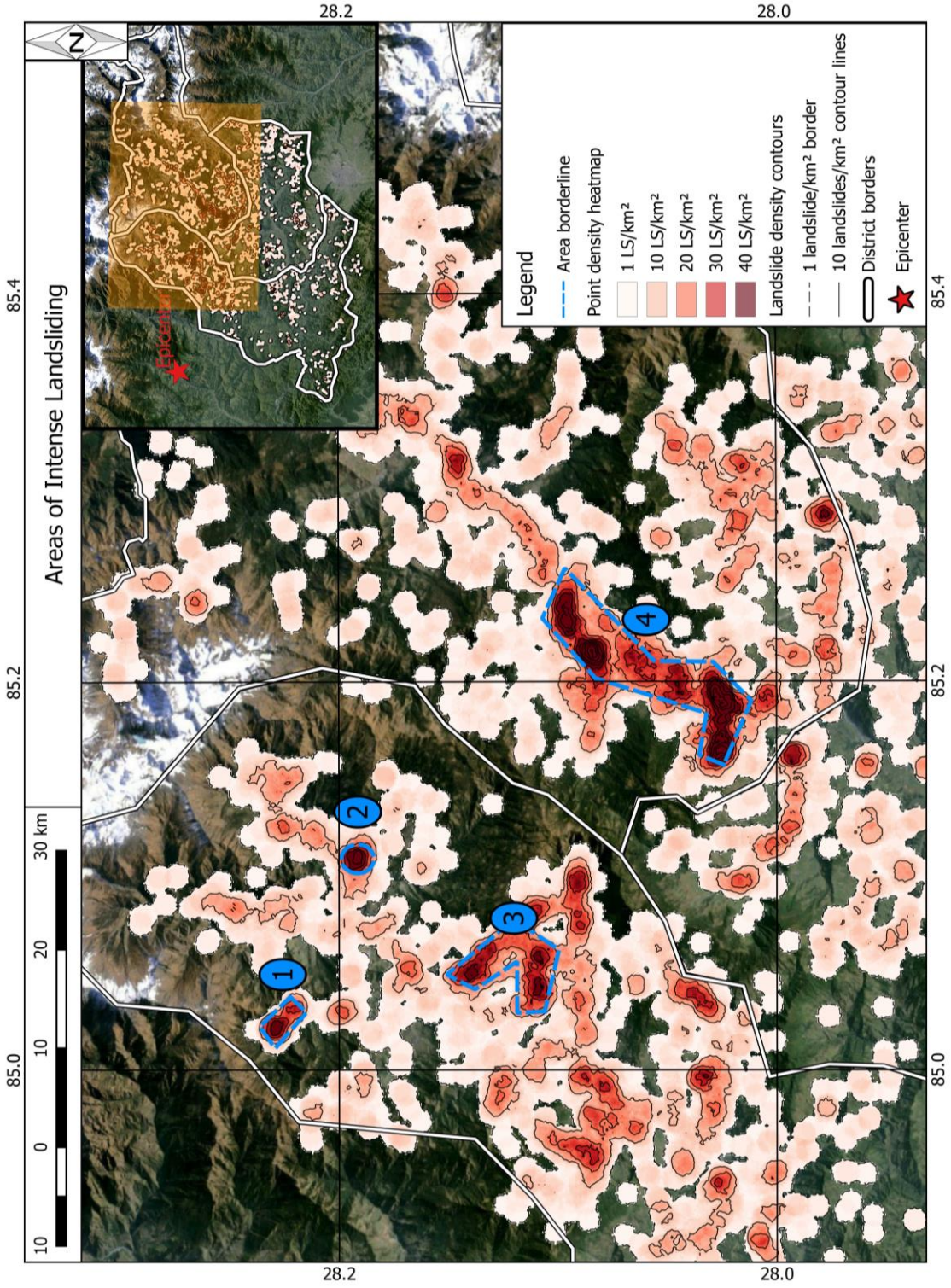

Fig. 42: Location of areas of intense landsliding. Blue dashed lines mark borders of areas.

- **Slope angle:** Fig. 43 shows the number of landslides which occurred in each slope angle class divided by the area of this class for each AIL individually. These values are referred to as density and are given in landslides per square kilometer (LS/km²). The general trend of a higher landslide density at higher slope angles can be estimated, but especially in area 1 this trend is not very distinct. The reason for the general trend not being present in especially area 1 may be because of the comparably low amount of landslides within this area.

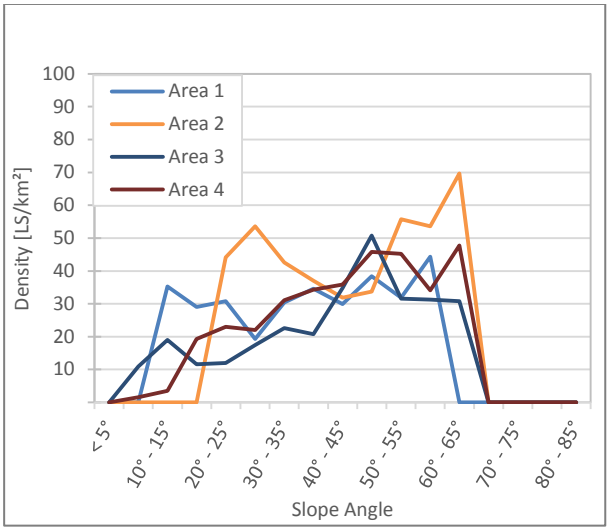

Fig. 43: AIL slope angle graphs, for each AIL a separate graph is displayed, the graphs indicate the number of landslides which occurred in each slope angle class (within the AIL) divided by the area of this class (within the AIL). These values are referred to as density and are given in landslides per square kilometer (LS/km²).

- **Slope aspect:** Fig. 44 shows the number of landslides which occurred in each slope aspect class divided by the area of this class for each AIL individually. These values are referred to as density and are given in landslides per square kilometer (LS/km²). Area 4 shows a trend of a higher susceptibility for landslides happening on south trending slopes. Areas 1 and 2 show this trend on west trending slopes. By combining these two trends, the overall trend in the research area can be seen, namely the higher susceptibility for landslides to occur on south and west trending slopes.

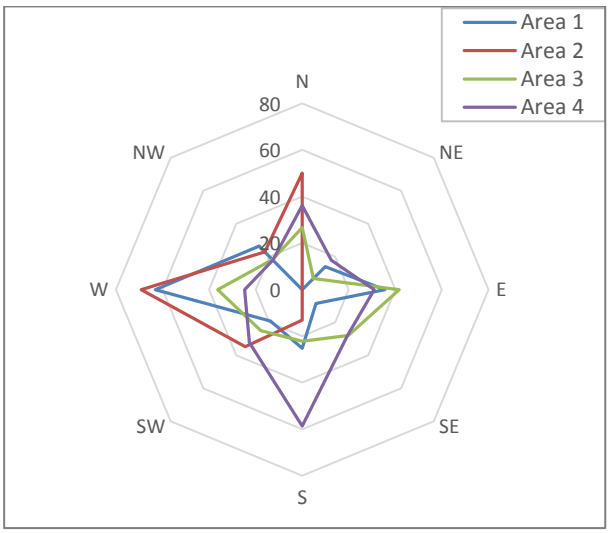

Fig. 44: AIL slope aspect spider diagram, for each AIL a separate graph is displayed, the graphs indicate the number of landslides which occurred in each slope aspect class (within the AIL) divided by the area of this class (within the AIL). These densities are given in landslides per square kilometer (LS/km²).

- **Elevation:** Fig. 45 shows the number of landslides which occurred in each elevation class divided by the area of this class for each AIL individually. These values are referred to as density and are given in landslides per square kilometer (LS/km²). In these graphs, no obvious pattern is present due to the different elevations of each of these AIL.

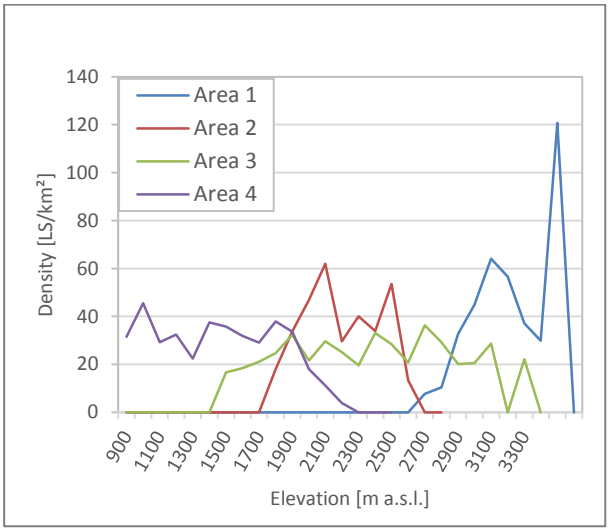

Fig. 45: AIL elevation graphs; for each AIL a separate graph is displayed, the graphs indicate the number of landslides which occurred in each elevation class (within the AIL) divided by the area of this class (within the AIL). These values are referred to as density and are given in landslides per square kilometer (LS/km²).

- **Geology:** Fig. 46 a and b show the number of landslides which occurred in each geological formation divided by the area of this formation for area 2 and 3. These values are referred to as density and are given in landslides per square kilometer (LS/km²). The reason why area s 2 and 3 were chosen is that in difference to areas 1 and 4, they have changing geologies. This means that they have almost the same conditions regarding ground slip, PGA, elevation, and such, the only exception being the geology. Fig. 46 a indicates a much higher susceptibility for landsliding in the na formation than in the hx formation. Fig. 46 b indicates a much higher susceptibility for landsliding in the kgn formation than in the kn formation. These figures confirm the high influence of the geology on the landslide susceptibility.

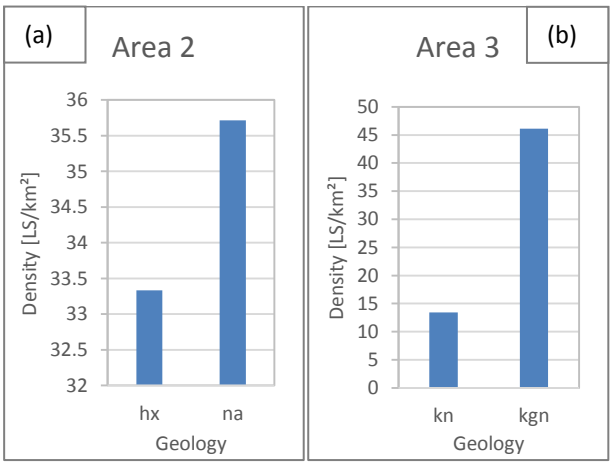

Fig. 46: AIL geology barplots; (a) AIL geology barplot of area 2, the bars indicate the number of landslides which occurred in the geological formations of area 2 divided by the area of these formations (within area 2); (b) AIL geology barplot of area 3, the bars indicate the number of landslides which occurred in the geological formations of area 3 divided by the area of these formations (within area 3); all values are referred to as density and are given in landslides per square kilometer (LS/km²);

4.4 Derivative Maps

For better interpretation of the data, a number of maps was generated, displaying data and results. Most of them are displayed on a Google Earth basemap, but some are on different kinds of maps, such as a ground slip magnitude map or a geological map. Also a density heatmap was generated, which gives the number of landsides within a circle shaped area of one square kilometer. All these maps present the data in their geographical relationship, which can give useful information like where most of the affected roads were located or it allows geological interpretations by displaying the landslide density on top of a geological map. The maps using the landslide density visualize that the number of landslides increases significantly north of 28° N and they mostly occur in the two major valleys there. According to the density heatmap, by far the highest landslide density is in the main valley in the southwestern part of Rasuwa (highest count: 91 landslides). The second highest landslide density is in the main valley in the northern part of Dhading. Evident is that the highest landslide density occurred in the bigger valleys with steep slopes and ground slip magnitudes exceeding 3.0 m. These parameters definitely apply for the southwestern part of Rasuwa.

- **Earthquake induced or reactivated landslides:** In Fig. 47, the earthquake induced and the pre – existing but reactivated landslides are plotted on a geographical basis. In addition to the fact that most landslides are earthquake induced ones, Fig. 48 visualizes that most of the pre – existing but reactivated landslides are in the southwestern part of Rasuwa, just where most landslides of the entire research area occurred. In contrast to the number of the reactivated landslides, most earthquake induced landslides occurred in the northern part of Dhading.

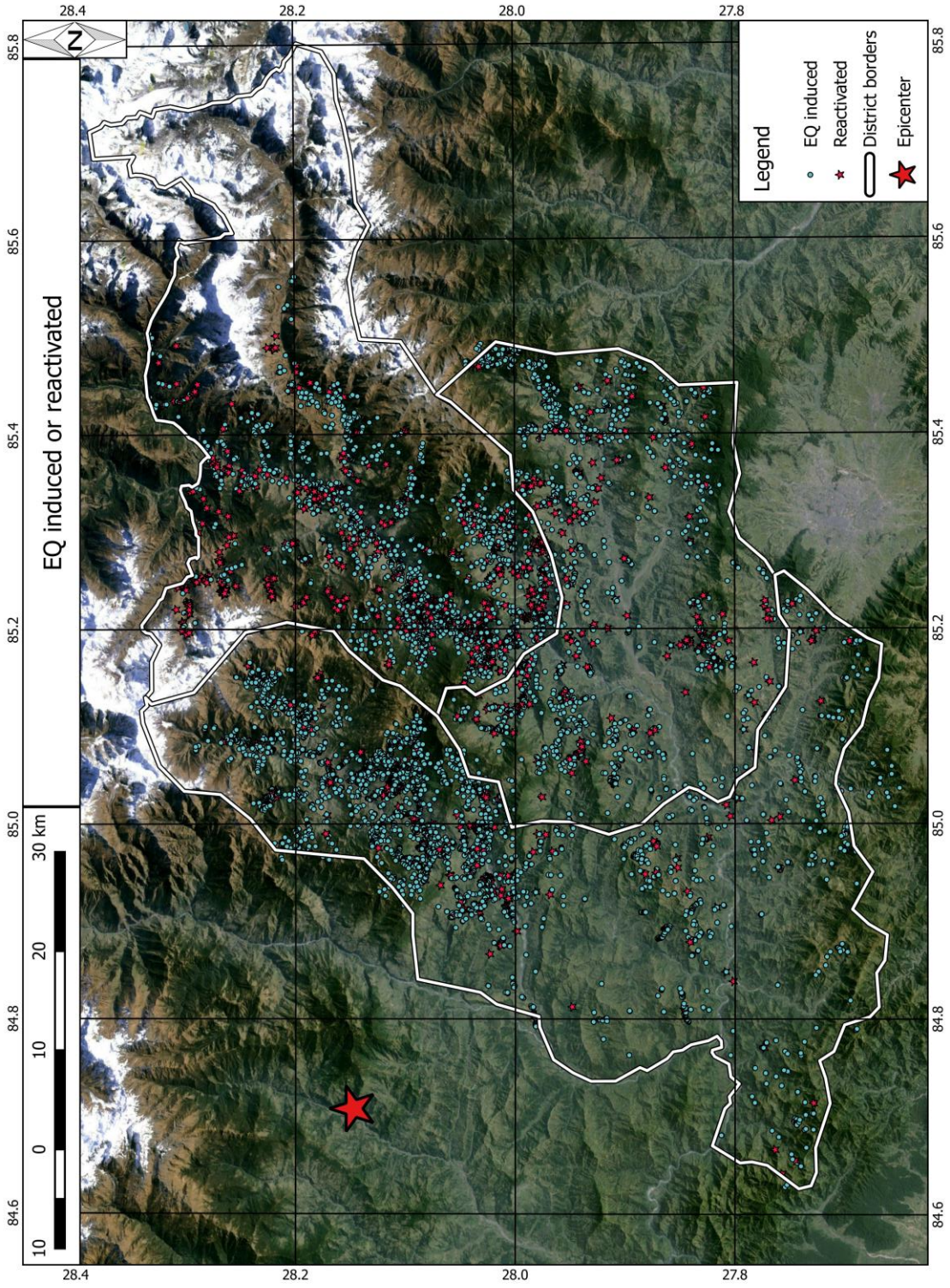

Fig. 47: Map of EQ induced or pre – existing but reactivated landslides.

- **Surface area:** In Fig. 48, the surface area of the landslides is plotted on a geographical basis. The majority of landslides have a comparably small surface area and it increases in direction to the High Himalaya. The abrupt increase of their surface area north of 28° N makes it almost possible to draw a line where the big landslides start. This trend is due to the increasing elevation, slope angle and slope relief to the north.

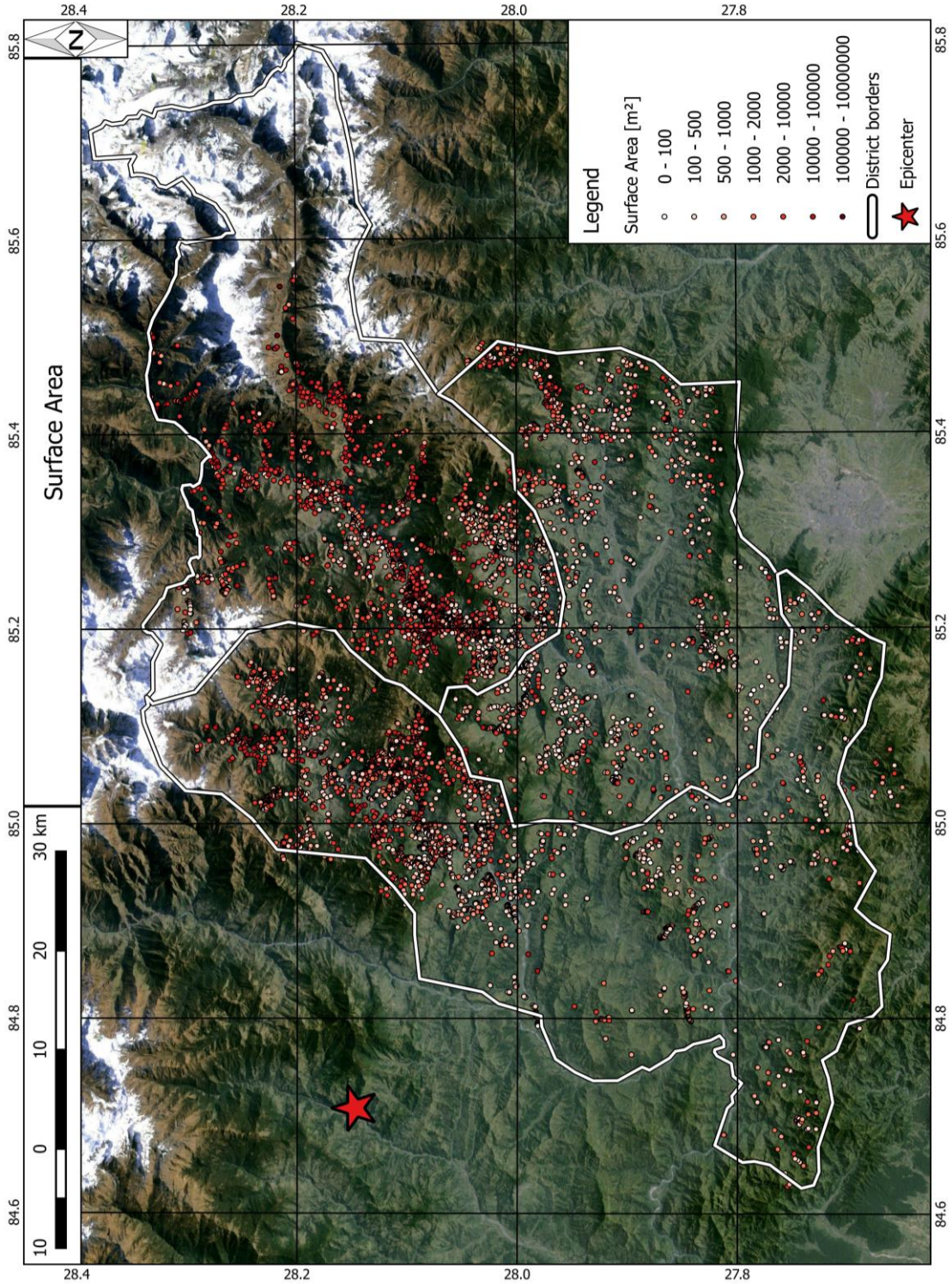

Fig. 48: Map of surface area of landslides.

- **Slope angle:** In Fig. 49, the slope angle of the slopes on which landslides occurred is plotted on a geographical basis. The map shows that landslides with steep slope angles are mostly in the northern part of the researched area. The domination of orange colored dots means that the majority of landslides occurred on a slope angle of approximately 40°. The increase of the slope angle to the north is due to the higher topography there.

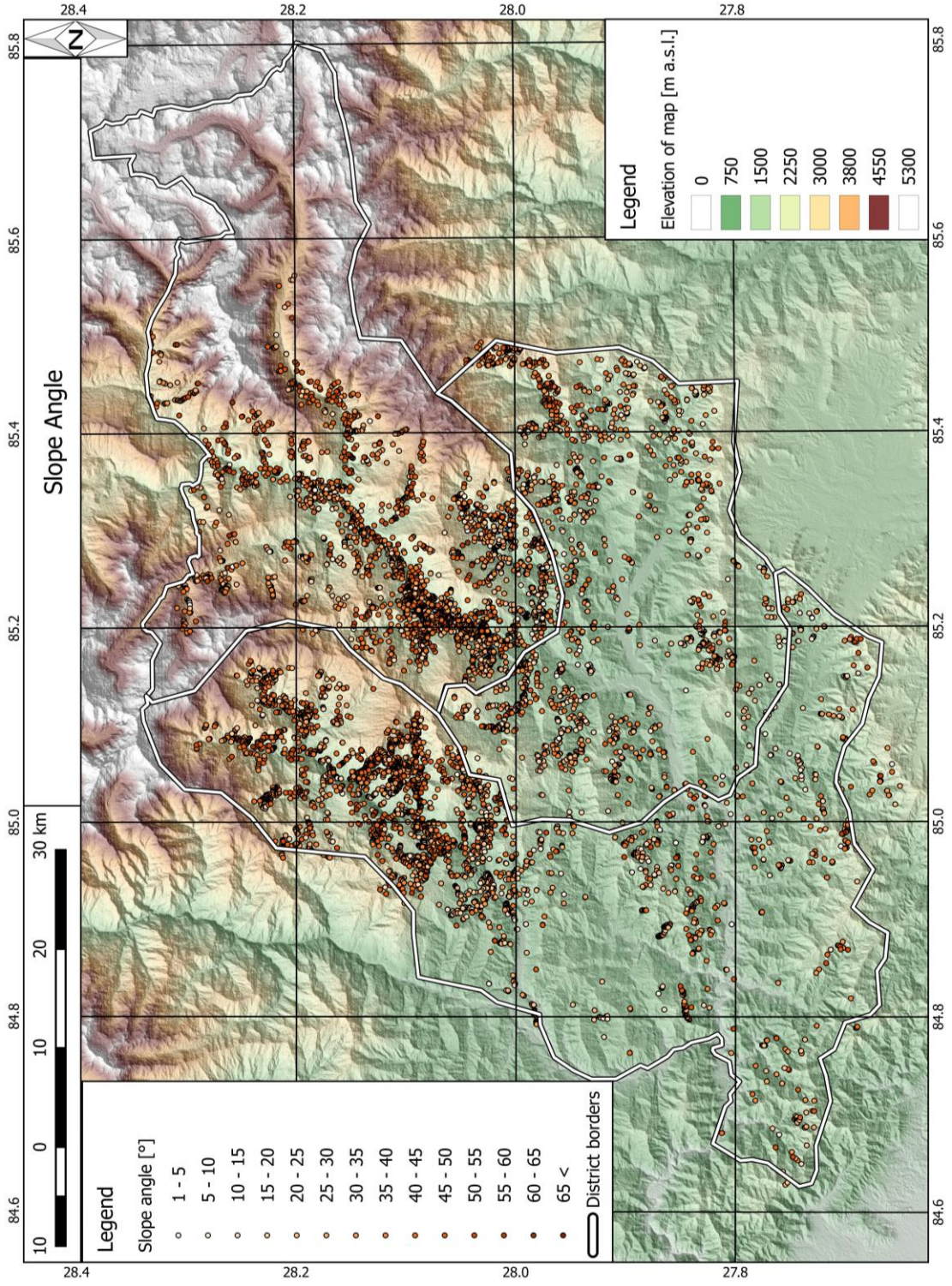

Fig. 49: Map of slope angle of slopes on which landslides occurred.

- **Geology:** In Fig. 50, the Geological Map of Nepal, 1994, is overlain by the landslide density. The highest density can be found in the Kuncha group (kn) and especially in the Augen gneisses and mica granites occurring in the Kuncha Group and Nawakot Group (kgn). This indicates the high susceptibility for landslides to occur in these two formations.

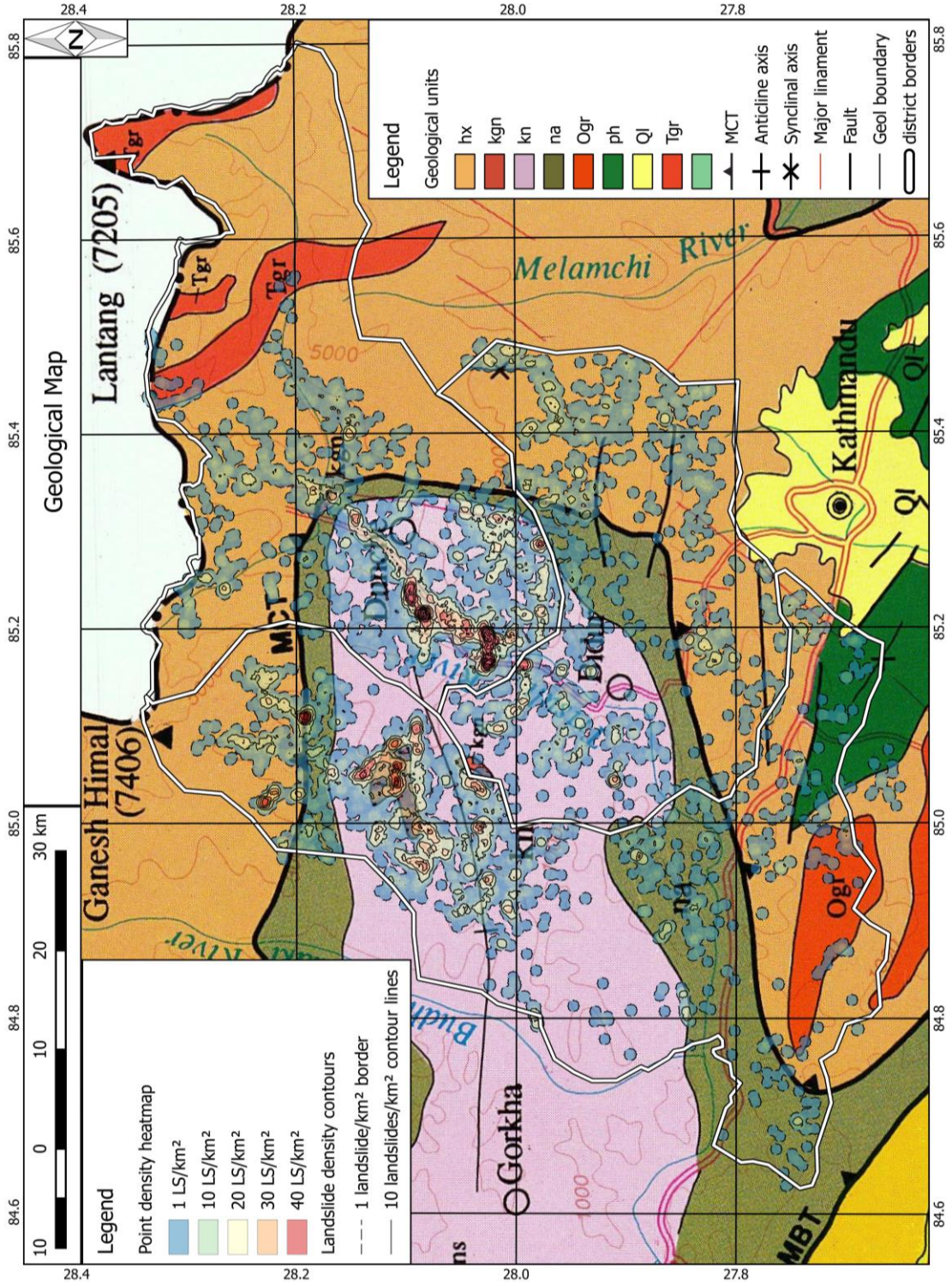

Fig. 50: Geological map: Geological Map of Nepal, 1994 overlain with the landslide density heatmap.

- **Slope aspect:** In Fig. 51 the slope aspect map and the density map are displayed. Also the slope aspect diagram is included. This map displays the trend of landslides to occur preferably on southern and western slopes.

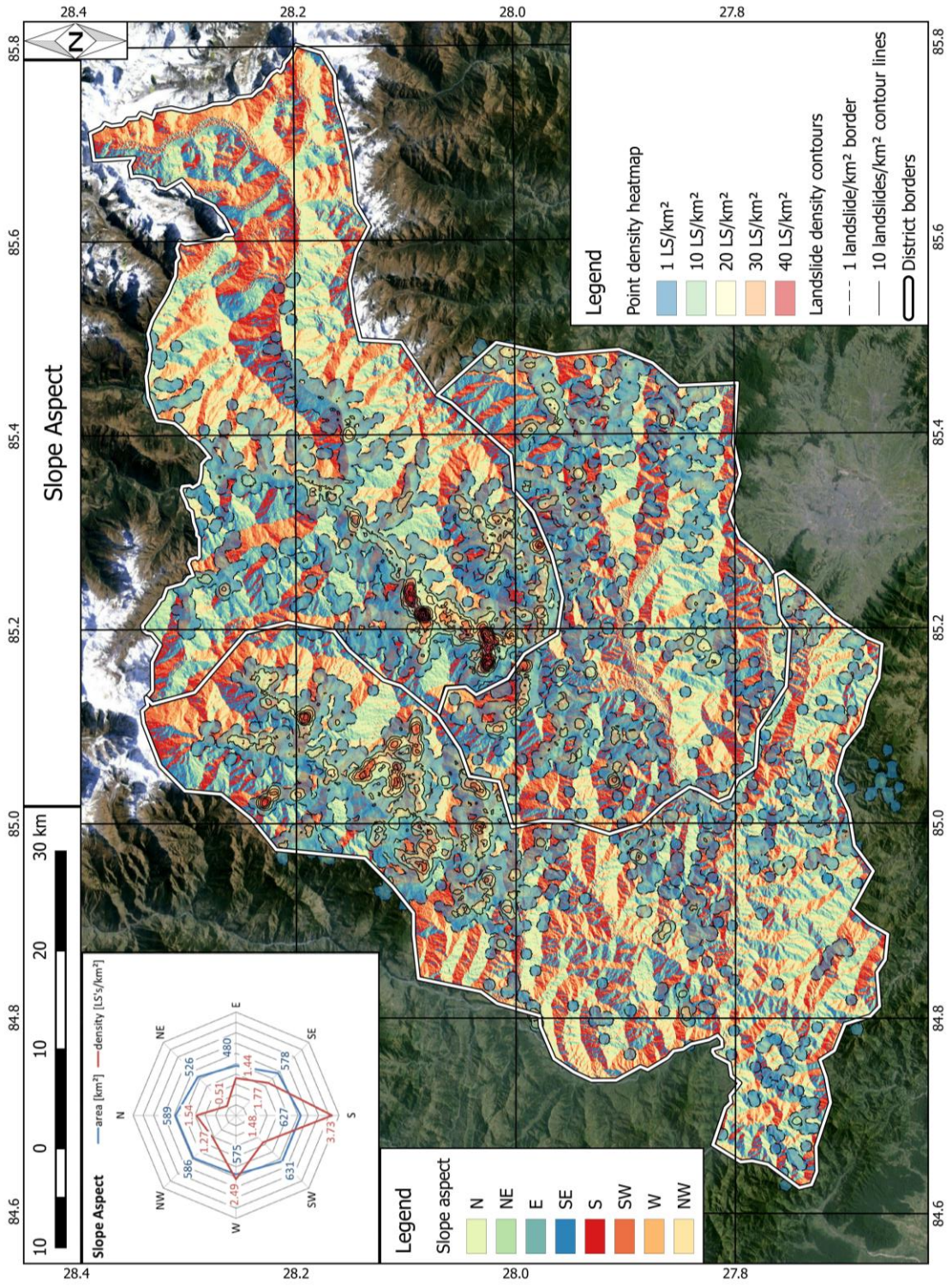

Fig. 51: Slope aspect map. The slope aspect diagram is in the upper left corner included.

- **Slope relief:** In Fig. 52, the slope angle of the landslides is plotted on a geographical basis. Not surprisingly, the slope relief increases to the north in direction to the High Himalaya. The slope relief in the southern part of Dhading and almost all of Nuwakot is rather small and around 500 m, whereas in Rasuwa and northern Dhading it increases to more than 2000 m. Further on, the map displays the positive correlation between the slope relief and the surface area of the landslides.

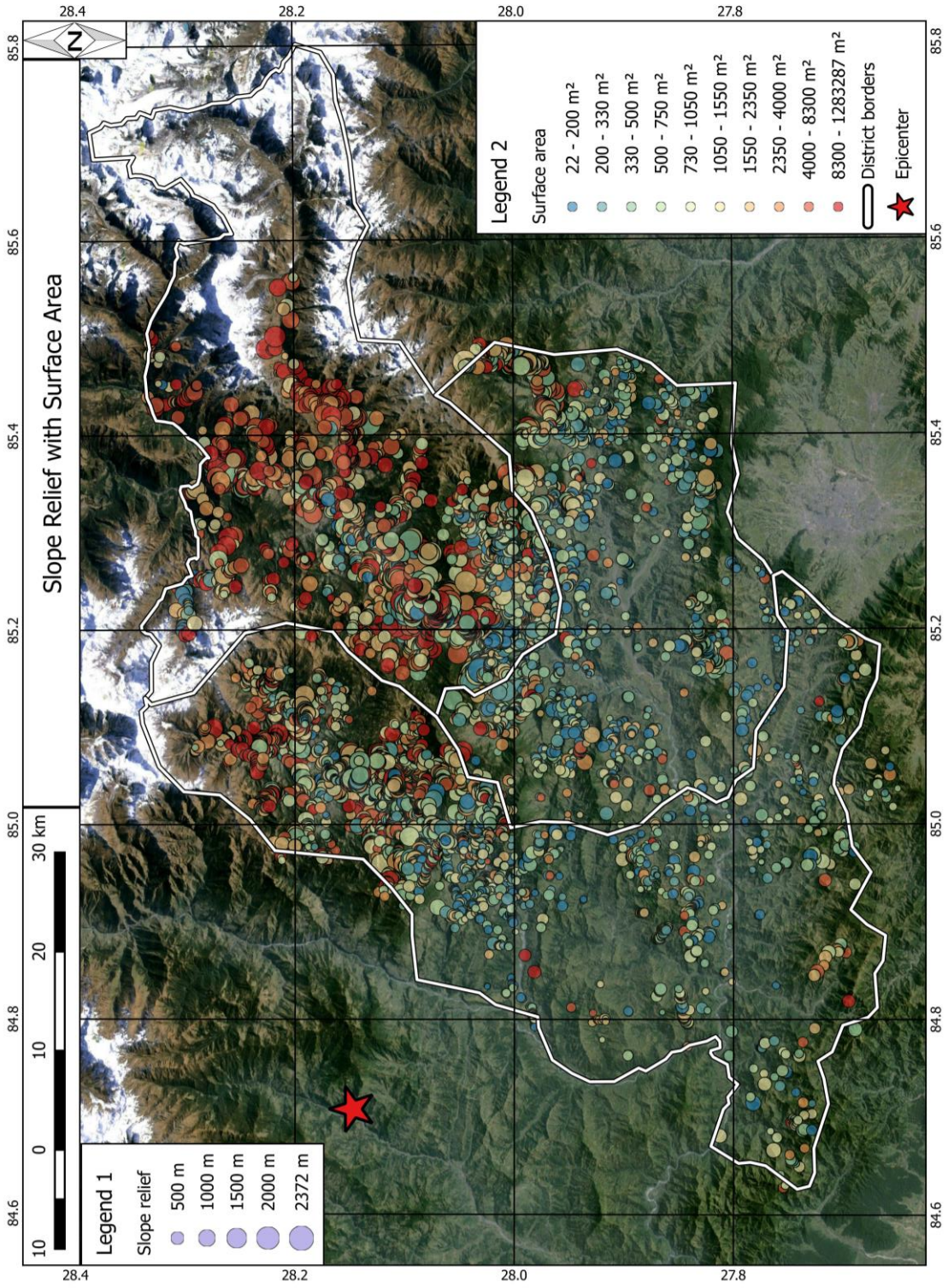

Fig. 52: Map of slope relief in correlation with landslide surface area.

- **Distance to epicenter:** In Fig. 53 the landslides are plotted regarding their distance to the epicenter. No distinct trend is detectable.

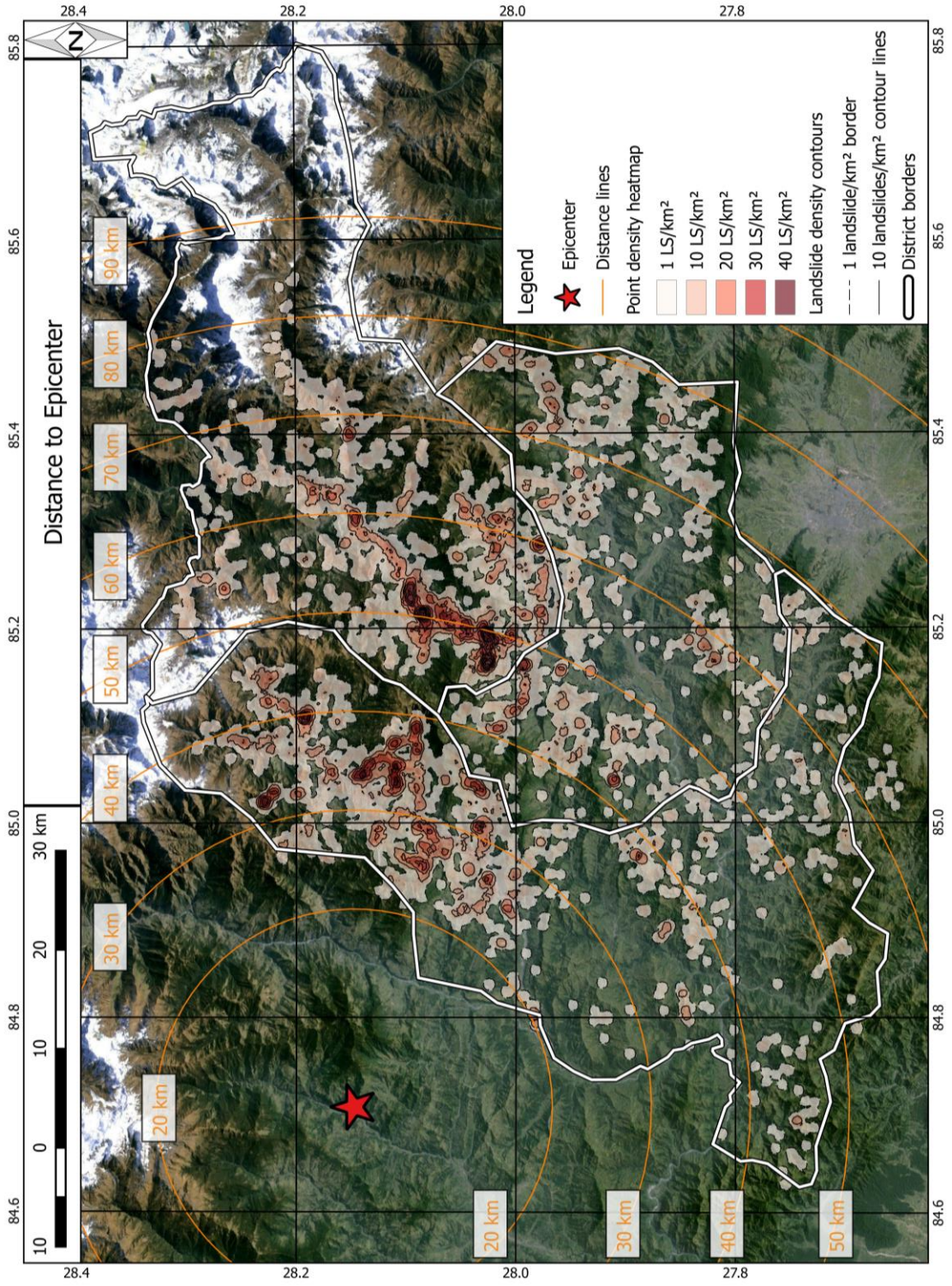

Fig. 53: Map of distance from epicenter.

- **Affected infrastructure:** Fig. 54 displays the affected infrastructure on a geographical basis. Also the density heatmap is displayed. This map visualizes that by far the highest amount of affected infrastructure is in the southwestern part of Rasuwa, exactly where also the highest landslide density was detected (228 roads, and 14 villages). This effect may be due to the highly inhabited area being there regardless of the steep slopes of this area.

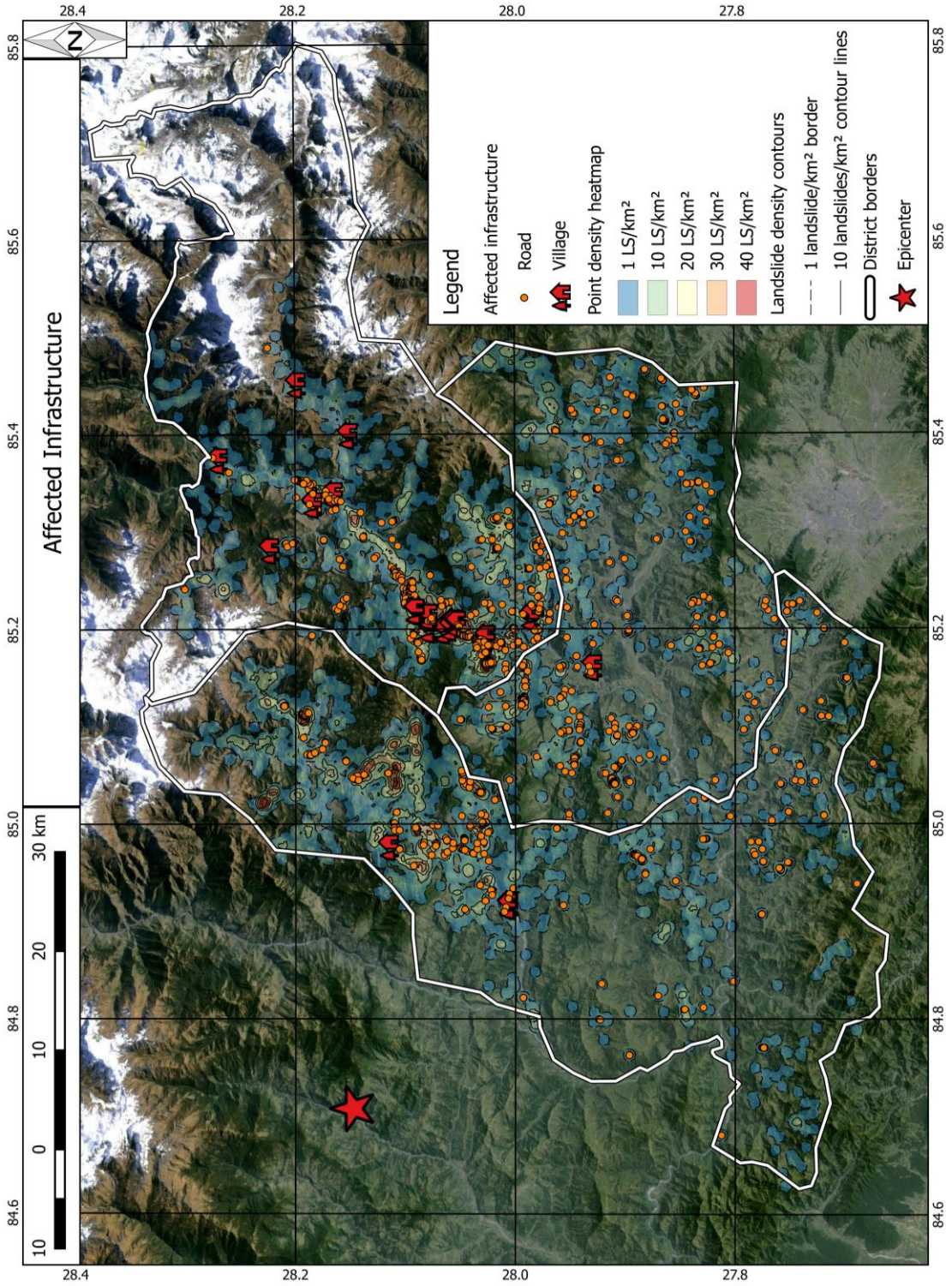

Fig. 54: Map of affected infrastructure. In addition to the infrastructure marks, the landslide density heatmap is pictured.

- **Elevation:** Fig. 55 shows the elevation map and the landslide density heatmap. An increase of the landslide density with the increase of elevation to the north until a certain point, namely at approximately 28.1° N, can be observed.

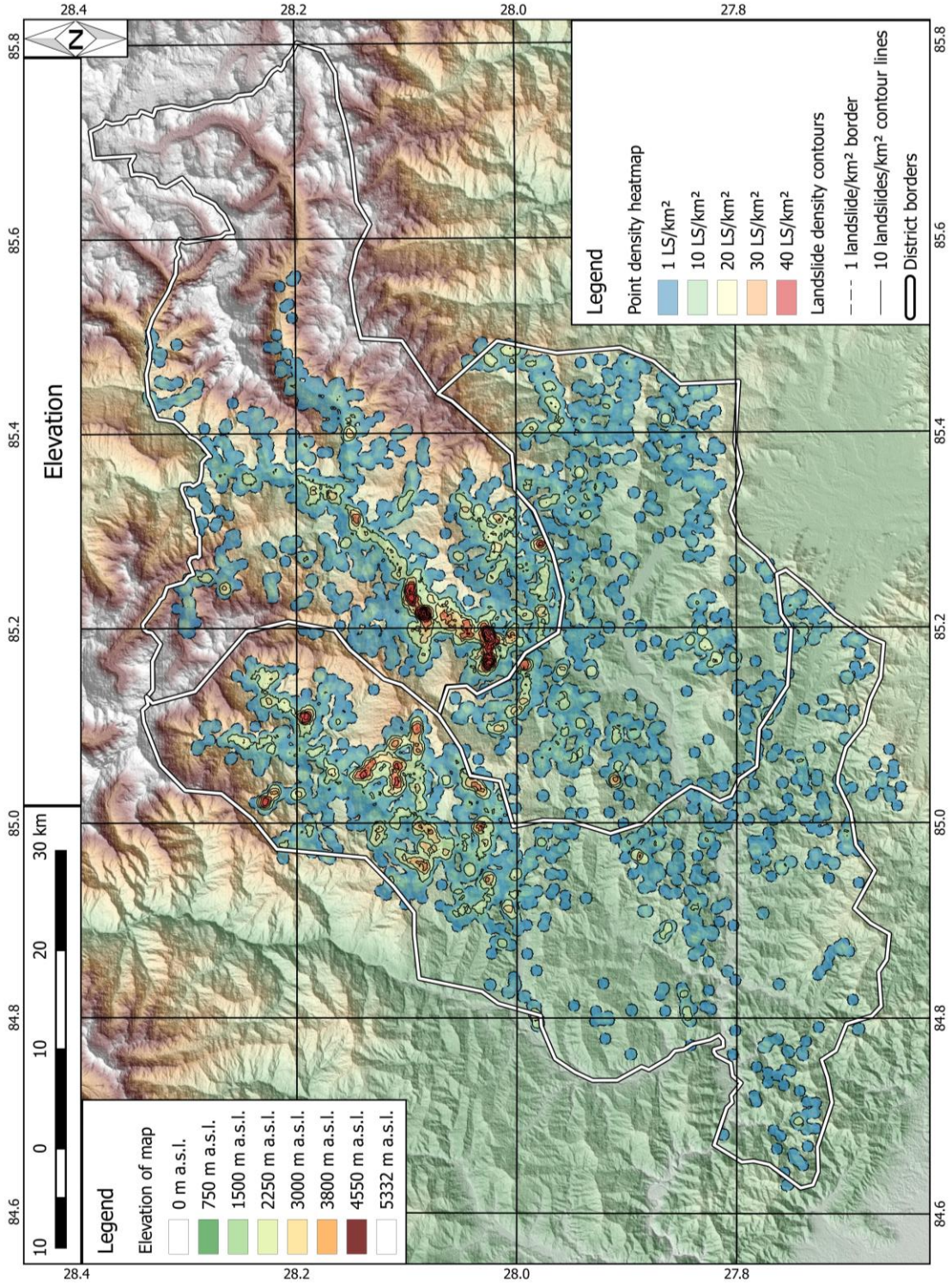

Fig. 55: Elevation map.

- **Ground slip magnitude:** In Fig. 56, the ground slip magnitude map (after Galetzka et al., 2015) is overlain by the landslide density heatmap. Most of the landslides occurred in the area where the magnitude was in the range of 2 to 5 m. However since the ground slip magnitude is not the only influencing factor, the highest density did not occur in the area with the highest ground slip, but where high magnitudes are present combined with high topographies.

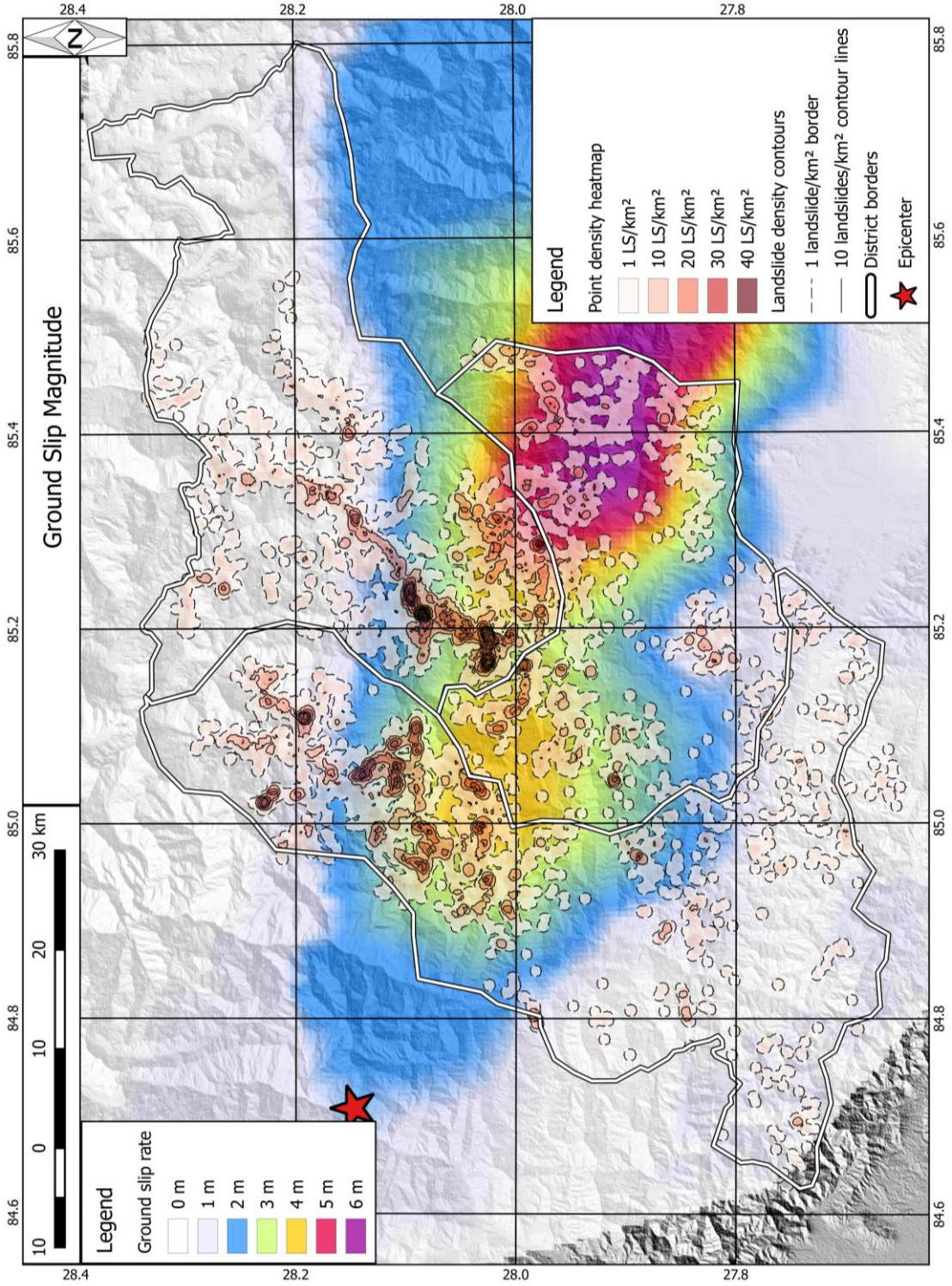

Fig. 56: Map of ground slip magnitude. The magnitude values are based on Galetzka et al. (2015).

- **PGA:** Fig. 57 shows the peak ground acceleration (Earthquake Damage Analysis Center, 2015) overlain with the landslide density. It illustrates that most of the landslides occurred in the area where the PGA was higher than 0.3 g. However no real trend between the landslide density and the PGA exceeding this value is detectable (the landslide density does not increase in the area with PGA > 0.8 g).

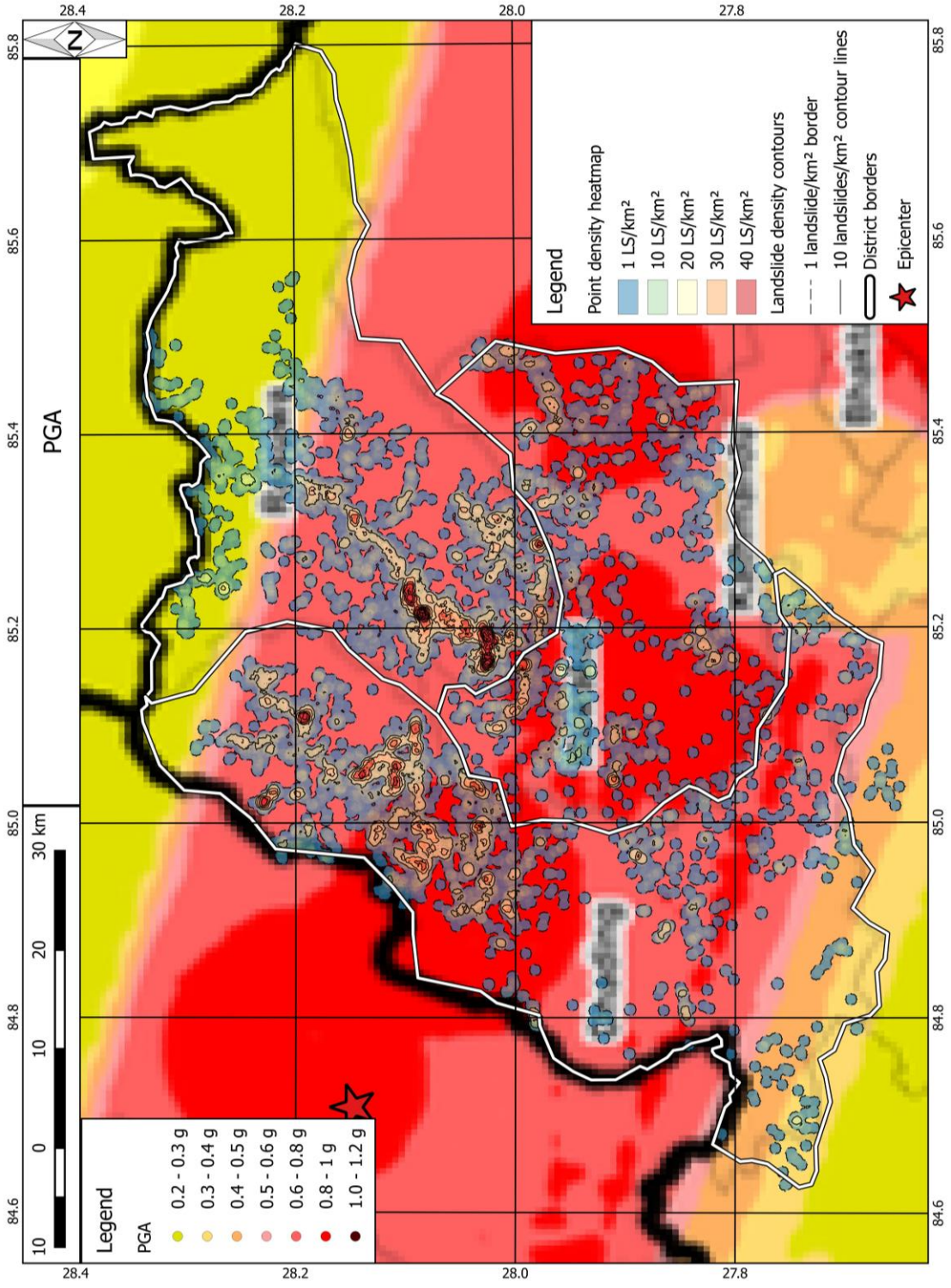

Fig. 57: PGA map. The PGA map from the Earthquake Damage Analysis Center (2015) is used as a basemap.

4.5 Field reconnaissance

The main goal of the field investigation was to determine whether the gathered remote sensing data is representative for the research area. As can be seen in Fig. 58 to Fig. 61, the ground taken photographs look almost the same as the once from Google Earth Pro. The differences are mainly due to the reshaping of the landslides during the monsoon season. As also displayed in these figures, all the outlines of the landslides are visible, showing the easy and precise way of the performance of measurements. The only two exceptions of these precise measurements occurred either when areas were overloaded with landslides or almost entire flanks slid, so that a differentiation between individual landslides was not possible, or when the required resolution of imagery was not available. Hence dealing with areas overloaded by landslides would have been even more difficult in the field and high resolution imagery was available for almost all areas, a high accuracy and reliability of the GIS based data with the site conditions could be approved. Another benefit of Google Earth Pro is that you can map landslides even at very remote places, which you cannot reach via car or by foot.

Fig. 58: (a) Ground taken photograph 1 vs. (b) Google Earth Pro screenshot; (b) showing high correlation of the Google Earth Pro imagery with the site conditions. Images taken at position 28.07768° N, 85.25085° E; Google Earth Pro Image © 2016 Digital Globe and 2016 CNES / Astrium.

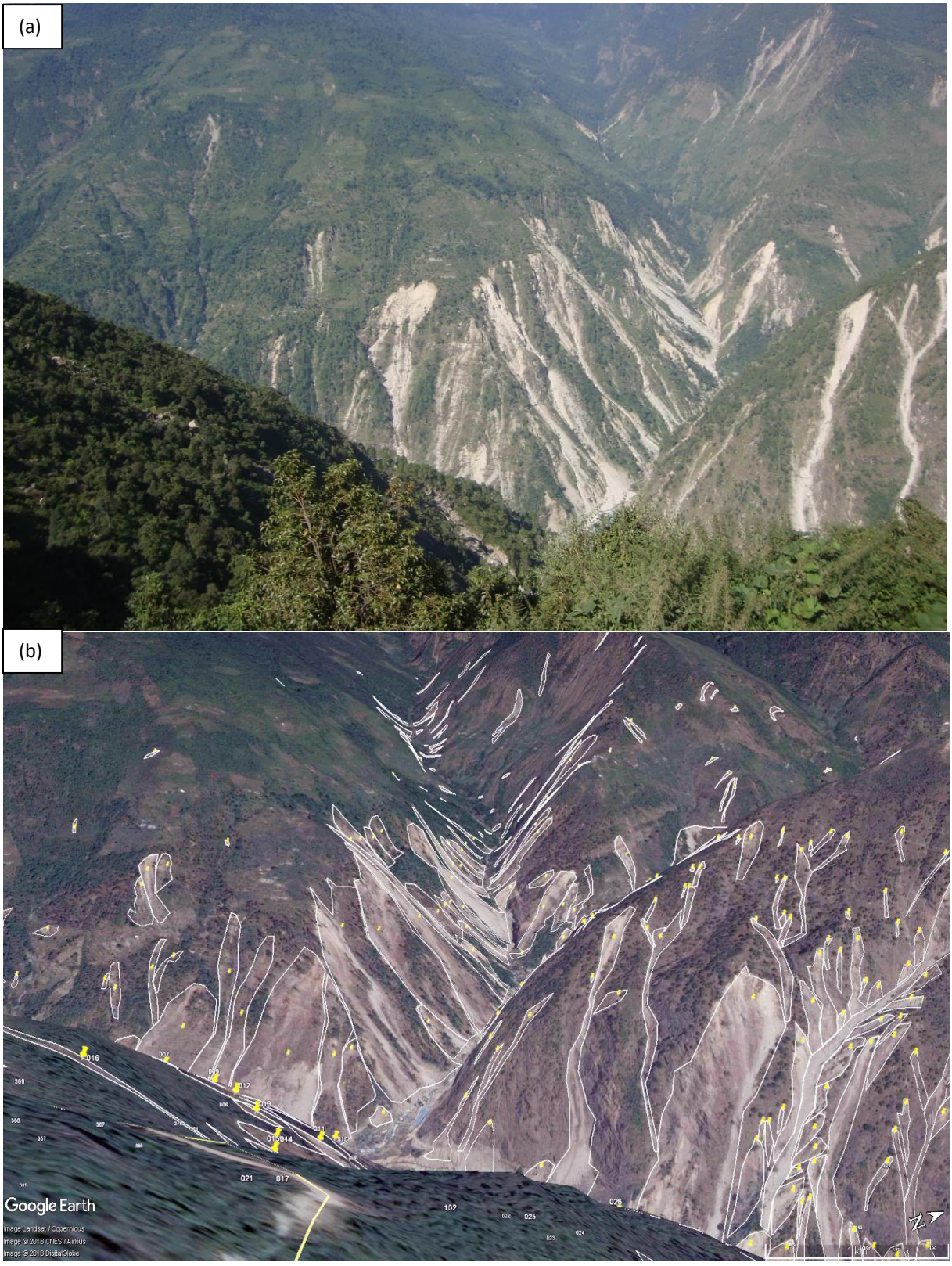

Fig. 59: (a) Ground taken photograph 2 vs. (b) Google Earth Pro screenshot; (b) showing high correlation of the Google Earth Pro imagery with the site conditions. Images taken at position 28.06822° N, 85.22652° E; Google Earth Pro Image © 2016 Digital Globe and 2016 CNES / Astrium.

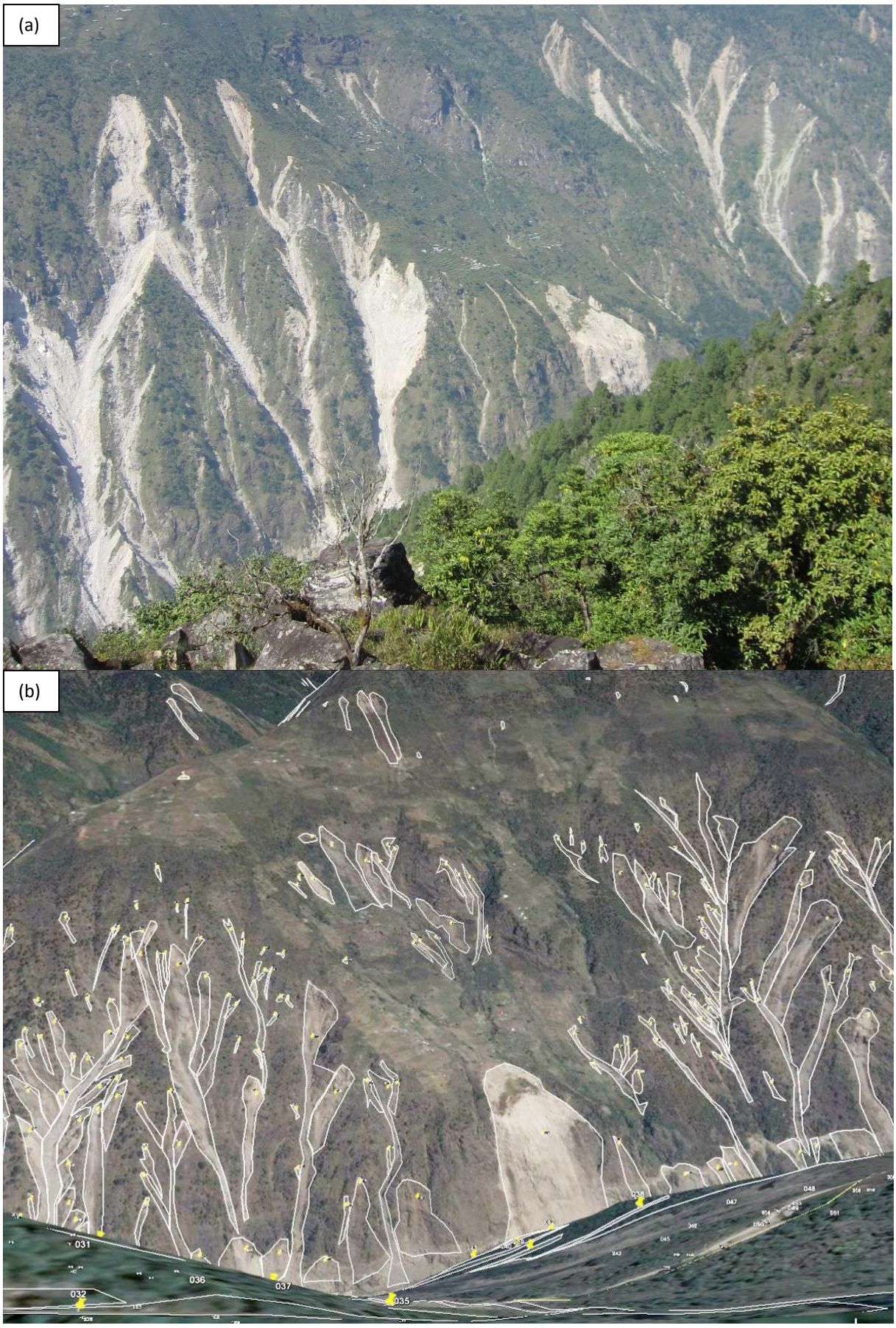

Fig. 60: (a) Ground taken photograph 3 vs. (b) Google Earth Pro screenshot, showing high correlation of the Google Earth Pro imagery with the site conditions. Images taken at position 28.06623° N, 85.22383° E; Google Earth Pro Image © 2016 Digital Globe and 2016 CNES / Astrium

Fig. 61: (a) Ground taken photograph 4 vs. (b) Google Earth Pro image after the monsoon and (c) Google Earth Pro image after earthquake and before monsoon showing high correlation of the Google Earth Pro imagery with the site conditions and the high influence of the monsoon and the date of the used imagery. Images taken at position 28.06818° N, 85.22649° E; Google Earth Pro Images © 2016 Digital Globe and 2016 CNES / Astrium.

During the field investigation, two different types of landslides could be observed. The first ones were earthquake triggered landslides, which happened during or immediately after the earthquake and can be directly related to the earthquake shaking. Secondly, there were monsoon triggered landslides. As Nepal is on the southern side of the Himalaya, the monsoon influences the climate strongly during the summer months and adds a lot of water to the soil. The monsoon triggered landslides happened because of this high or even over - saturation of the soil.

As the earthquake occurred only a few weeks before the monsoon season (starting in June), the soil was mostly dry. Therefore, the earthquake triggered landslides occurred mainly on steep slopes with low overburden or they were small rockfalls, topples or slides on fault surfaces (Fig. 62 and Fig. 63). The water saturation of the soil was too low for deep seated landslides. These landslides occurred very often close to roads, as they were cut into the partly steep hillsides without any proper geotechnical support methods. Often the landslide crown was situated at the valley side edge of the roadcut or uphill of the cut, spilling onto the road. Either of these situations can block or even destroy the road. Shown in Fig. 63 is the high influence of the landslides on the infrastructure, not only on roads and houses, but also on water power plants. Besides the infrastructure causing landslides, many landslides occurred due to topography in steep V – shaped, river formed valleys. In addition to all landslides, a lot of tension cracks could be observed across the whole research area.

The second type of landslides occurred during the following monsoon season. Most of them were large landslides, where the loosened rock and soil, which was saturated by the ongoing rain, started moving. This effect was supported by the open cracks created by the earthquake shaking. Because of the by water reduced friction angle, the landslide toe moves much further and needs a less steep slope to be stopped than the landslides happening in dry soil, and so the monsoon caused landslides to become much bigger. As described from local villagers, these landslides moved continuously a few meters per day and can therefore be classified as earthflows. These landslides destroyed a huge amount of infrastructure just a few weeks after the earthquake did. This is, especially in Nepal, very serious, as all the essential supply material (except from drinking water) are transported on the main roads and most of the times only one major road is present within huge valleys.

Fig. 62: Panorama picture of many small landslides in Rasuwa taken at Trishuli Highway (28.04649° N, 85.22331° E), view from SW (left edge) to NE (right edge). The high influence of the valleys on the landslide density can be seen (high density in lower, steeper, V – shaped valley part, lower density in upper, flatter part). Based on field reconnaissance it is known that most landslides are small rockfalls, topples and slides on fault surfaces or slides on steep slopes with low overburden

Fig. 63: Images showing the influence of earthquake induced landslides on infrastructure; (a) Influence on houses (foreground), rock slide on fault surface (background) (27.93446° N, 85.93931° E); (b) Influence of rockfall onto bridge / road (27.93077° N, 85.93637° E); (c) Influence on waterpower plant pipe (27.93386° N, 85.93732° E)

During the field reconnaissance, four big monsoon activated landslides blocking the Araniko Highway were observed, three of them were incredibly large. The first was at positon 27.90636° N and 085.92098° E, destroying houses and blocking the road (Fig. 64 a and b). The second and third were next to each other at position 27.93661° N and 85.94155° E (Fig. 64 b, c and d). Locals reported that these landslides occurred during the monsoon season and moved approximately 2 m down slope every day. The forth landslide happened a few hundred meters before the Chinese border in the village Kodari (Fig. 64 f) (27.971419° N, 85.961754° E). The first three landslides were earthflows, the forth was a rockslide, destroying almost the whole village and blocking the road for many months.

Fig. 64: Landslides triggered by the earthquake and activated by the monsoon at Araniko Highway. (a) source area first landslide; (b) deposit area first landslide, blocked road (reopened on picture) and destroyed houses; (c) and (d) second landslide source and deposit area, blocked road and destroyed buildings, bulldozer marks former road; (e) parts of third landslide (front) and source area of second landslide (background); (f) forth landslide in Kodari, destroying buildings and blocking road for several months.

5 Discussion and Conclusion

The Gorkha (Nepal) earthquake of April 25, 2015 has been the largest earthquake in this area since 1934. Approximately 8800 people were killed, tens of thousands were injured and thousands of buildings were destroyed. Due to strong ground shaking motions, thousands of landslides were triggered. Within the three districts Rasuwa, Nuwakot and Dhading, more than 8000 earthquake triggered landslides were identified and mapped.

Mapping on high resolution Google Earth Pro satellite imagery revealed 8330 earthquake triggered landslides which were further investigated and evaluated. By importing the mapping data into QGIS, geomorphometric and spatial landslide parameters were evaluated, including location data, surface area, slope angle, aspect ratio, geologic unit, slope aspect, slope relief, elevation and ground slip magnitude for each landslide. Besides, information about affected infrastructure (roads and villages) and whether the landslide was earthquake induced or pre – existing but reactivated, was collected. Finally, all the gathered datasets were statistically analysed, evaluated and plotted on diagrams and maps by using Microsoft Excel, R Studio and QGIS. A map including the landslide density and the peak ground acceleration (PGA) was added (Earthquake Damage Analysis Center, 2015). In addition to the remote sensing data evaluation, two weeks of field reconnaissance were performed to determine the reliability of the dataset and to gather information of the effects of the monsoon on the landslides and the landslide situation.

With 86%, the majority of the mapped landslides were earthquake induced. The most likely reason for the much higher number of earthquake induced landslides compared to pre – existing but reactivated landslides is the difficulty to spot pre – existing landslides on the used imagery. Approximately 50% of all landslides have a surface area of less than 1000 m². The resolution threshold and therefore the minimum area of landslides to be defined, was at approximately 200 m². Overall, 1034 roads and 25 villages were hit by earthquake triggered landslides and by far the highest number of infrastructure being influenced was in the southwestern part of Rasuwa (approximately 230 roads and 14 villages).The high number of landslides affecting infrastructure in the southwestern part of Rasuwa is thought to be because of various reasons. These include the high landslide density, the kind of terrain where the roads were built (steep slopes where landslides are likely to occur) and the high population density in contrast to the rest of Rasuwa or northern Dhading.

The most important factors influencing the occurrence of landslides include:

- The **ground slip magnitude** (after Galetzka et al., 2015): The highest landslide density lies between 3.0 m and 5.0 m of ground slip magnitude. The highest magnitude was approximately 6.5 m (Galetzka et al., 2015). The highest values of ground slip magnitude were situated north of Kathmandu, characterized by a predominantly flat topography. As the topography affects the landslide susceptibility significantly, this is the most likely reason for the decrease of the landslide density at the highest ground slip magnitudes.
- The **slope angle**: The slope angle has a strong effect on the landslide density. The highest numbers of landslides are located at slope angles between 35° and 40°, the highest landslide density between 55° and 60°. Based on the field reconnaissance, the earthquake induced landslides mainly happened on steep slopes with low overburden or were small rockfalls, topples or slides on fault surfaces. The trend of a higher landslide density happening on steeper slopes can be explained by steep slopes being more prone to the identified types of landslides.

- The **geology**: the highest susceptibility for landsliding was in the Augen gneisses and mica granites occurring in the Kuncha Group and Nawakot Group (kgn) and in the mainly shallow marine sediments of the Kuncha Group (kn). This effect is thought to be due to structural, textural and weathering properties.
- The **slope aspect**: It was observed that south and west facing slopes had a much higher susceptibility for landslides to occur. Various authors discovered similar trends and explained it with parameters which can increase the susceptibility for landsliding before the earthquake occurs by effecting the vegetation, the weathering, the degree of saturation or the rock mass strength (e.g. Guzzetti et al., 1999; Evans et al., 1999; Nagarajan et al., 2000; Yalcin, 2008). These factors include exposure to sunlight, drying winds, and discontinuities. Also, the ground slip direction may have an influence.

The data inter – relationships show that the landslide surface area has a positive correlation with the slope relief and the slope angle. This trend shows that at steeper slopes and/or at a higher slope relief, the surface area of the landslides increases. At higher slope angles, the difference between the friction angle of the landslide material and the slope angle is bigger, resulting in a higher driving force. This higher driving force increases the material displacement resulting in a higher surface area. At higher slope reliefs, the landslides become bigger as they have a longer way reaching the valley bottom. These facts explain the positive correlation of the surface area with the slope angle and the slope relief. Another data inter – relationship was determined between the surface area and the ground slip magnitude. There is a negative correlation between the two due to the highest magnitude being situated at flat topographies with flat slopes and small slope reliefs. The inter – relationship plots confirm that the slope relief and the slope angle increase with the elevation.

The performed two weeks of field reconnaissance showed a high correlation of the GIS based data with the actual site conditions. Therefore, the landslide inventory is highly reliable and can be used for further landslide statistics. Further on, it was examined that the monsoon affected the landslides and the landslide conditions strongly as it had already reshaped the earthquake triggered landslides and activated new ones. These new landslides moved a few meters per day and often seriously affected the infrastructure.

The gathered and analyzed data reflect the general behavior of the Himalayan area on earthquakes regarding the triggering of landslides. Based on the present dataset, hazard and risk assessments on dynamic and static slope stabilities can be performed and for example, hazard maps can be created. Implementation of the presented inventory into a greater inventory can contribute to the development of detailed hazard assessment campaigns on a regional scale.

6 References

Ader, T*., (*2012*),* Convergence rate across the Nepal Himalaya and interseismic coupling on the Main Himalayan Thrust: Implications for seismic hazard*,* Journal of Geophysical Research v. 117*, B04403, doi:10.1029/2011JB009071.*

ASTER GDEM is a product of METI and NASA

Ayalew, L., Kasahara, M., Yamagishi, H., 2011, The spatial correlation between earthquakes and landslides in Hokkaido (Japan), a GIS-based analysis of the past and the future. Landslides v. 8, v. 433-448.

Avouac, J. P., 2003, Mountain building, erosion, and the seismic cycle in the Nepal Himalaya, Advances in Geophysics v. 46, p. 1–80.

Bettinelli, P., J.-P. Avouac, M. Flouzat, F. Jouanne, L. Bollinger, P. Willis, and G. Chitrakar, 2006, Plate motion of India and Interseismic strain in the Nepal Himalaya from GPS and DORIS measurements, Journal of Geodesy v. 80, p. 567–589.

Bhusal, Y. R., 2012, National Population and Housing Census 2011: Central Bureau of Statistics, v. 01, p. 40

Bilham, R., 1995, Location and magnitude of the 1833 Nepal earthquake and its relation to the rupture zones of contiguous great Himalayan earthquakes. Curr. Sci. 69, 101–128.

Bollinger, L., Henry, P., and Avouac, J.P., 2006, Mountain building in the Nepal Himalaya: Thermal and kinematic model, Earth and Planetary Science Letters v. 244, p. 58–71

Bollinger, L., Sapkota, S.N., Tapponnier, P., Klinger, Y., Rizza, M., Van der Woerd, J., Tiwari, J.R., Pandey, R., Bitri, A., and Bes de Berc, S., 2014, Estimating the return times of great Himalayan earthquakes in eastern Nepal: Evidence from the Patu and Bardibas strands of the Main Frontal Thrust. Journal of Geophysical Research SolidEarth v. 119, doi:10.1002/2014JB010970.

Cattin, R., and Avouac, J. P., 2000, Modeling of mountain building and the seismic cycle in the Himalaya of Nepal. Journal of Geophysical Research v. 105, p. 13389–13407.

Chitrakar, G.R., Pandey, M.R. (1986). Historical earthquakes of Nepal. Bulletin Geological Society of Nepal 4, 7–8.

DeCelles, P. G., Robinson, D. M., Quade, J., Ojha, T. P., Garzione, C. N., Copeland, P., and Upreti, B. N., 2001, Stratigraphy, structure, and tectonic evolution of the Himalayan fold-thrust belt in western Nepal. Tectonics v. 20, p. 487–509.

Delcaillau, B. (1986). Dynamique et. evolution structurale du piemont frontal de lmalaya: les Siwaliks du Nepal oriental. Revue de geologie dynamique et de geographie physique v. 27, p. 319–337.

Earthquake Damage Analysis Center (EDAC) of the Bauhaus-University Weimar, according to the USGS PGA map versin 7, 2015.

Evans NC, Huang SW, King JP, 1999, The natural terrain landslide study, phases I and II. The Government of the Hong Kong Special Administrative Region, GEO Report v. 73.

Galetzka J., Melgar D., Genrich J. F., Geng J., Owen S., Lindsey E. O., Xu X., Bock Y., Avouac J.-P., Adhikari L. B., Upreti B. N., Pratt-Sitaula B., Bhattarai T. N., Sitaula B. P., Moore A., Hudnut K. W., Szeliga W., Normandeau J., Fend M., Flouzat M., Bollinger L., Shrestha P., Koirala B., Gautam U., Bhatterai M., Gupta R., Kandel T., Timsina C., Sapkota S. N., Rajaure S., Maharjan N., 2015, Slip pulse and resonance of the Kathmandu basin during the 2015 Gorkha earthquake, Nepal, Science v. 349, p. 1091-1095.

Guzzetti, F., Cardinali, M., Reichenbach, P., Carrara, A., 2000, Comparing landslide maps: a case study in the upper Tiber River Basin. Central Italy, Environmental Management v. 25, p. 247–363.

Guzzetti, F., Mondini, A.C., Cardinali, M., Fiorucci, F., Santangelo, M., Chang, K.T., 2012, Landslide inventory maps: new tools for an old problem. Earth-Science Reviews v. 112, p. 42-66.

Hansen, A., 1984a, Engineering geomorphology: the application of an evolutionary model of Hong Kong. Zeitschrift für Geomorphologie v. 51, p. 39–50.

Hansen, A., 1984b, Strategies for classification of landslides. In: Brunsden, D., Prior, D.B. (Eds.), Slope Instability. Wiley, New York, p. 523–602.

Harp E.L., Jibson R.W., 1995, Inventory of landslides triggered by the 1994 Northridge, California earthquake. US Geological Survey. http://pubs.usgs.gov/of/1995/ofr-95- 0213/plate1.gif

Harp .E.L, Jibson R.W., 1996, Landslides triggered by the 1994 Northridge, California, earthquake. Bulletin of the Seismological Society of America, Fharpv. 86(1B), p. 319–332.

Harp, E.L., Keefer, D.K., Sato, H.P., Yagi, H., 2011, Landslide inventories: the essential part of seismic landslide hazard analyses. Engineering Geology, v. 122, p. 9-21.

Hashash, Y. M. A., Tiwari, B., Moss, R. E. S., Asimaki, D., Clahan, K. B., Kieffer, D. S., Dreger, D. S., Macdonald, A., Madugo, C. M., Mason, H. B., Pehlivan, M., Rayamajhi, D., Acharqa, I., and Adhikari, B., 2015, Geotechnical Field Reconnaissance: Gorkha (Nepal) Earthquake of April 25 2015 and Related Shaking Sequence. Geotechnical Extreme Event Reconnaissance, No. GEER-040, v. 1.1, p 27 – 93.

Hung, J.J., 2000, Chi-Chi earthquake induced landslides in Taiwan, International Workshop on Annual Commemoration of Chi-Chi Earthquake, September 18–20, 2000: Nat. Center for Research

Johnson, M. R. W., 2005, Structural settings for the contrary metamorphic zonal sequences in the internal and external zones of the Himalayan. Journal of Asian Earth Sciences, v. 25, p. 695-706.

Kamp, U., Growley, B. J., Khattak, G. A., Owen, L. A., 2008, GIS-based landslide susceptibility mapping for the 2005 Kashmir earthquake region. Geomorphology, v. 101, p. 631-642.

Keefer D.K., 1984, Landslides caused by earthquakes. Bulletin of the Geological Society of America v. 95(4), p. 406–421

Keefer, D.K., 1989, The Loma Prieta, California earthquake of October 17, 1989-landslides. U.S. Geological Survey Professional Paper, v. 1551-C, 185 pp.

Keefer, D.K., 2000, Statistical analysis of an earthquake-induced landslide distribution of the 1989 Loma Prieta, California event. Engineering Geology, v. 58, p. 231-249.

Khazai B., Sitar N., 2004, Evaluation of factors controlling earthquake-induced landslides caused by Chi-Chi earthquake and comparison with the Northridge and Loma Prieta events. Engineering Geology, v. 71(1–2), p. 79–95

Larson, K., Bürgmann, R., Bilham, R., Freymueller, J.T., 1999, Kinematics of the India–Eurasia collision zone from GPS measurements. Journal of Geophysical Research v. 104, p. 1077–1093.

Lave, J., and Avouac, J. P., 2000, Active folding of fluvial terraces across the Siwaliks Hills, Himalayas of central Nepal.Journal of Geophysical Research v. 105, p. 5735–5770.

Le Fort, P., 1975, Himalaya: the collided range: Present knowledge of the continental arc, American Journal of Science 275A, 1–44.

Li Y., Chen G., Tang C., Zhou G., Zheng L., 2012, Rainfall and earthquake-induced landslide susceptibility assessment using GIS and Artificial Neural Network. Natural Hazards and Earth System Science, v.12, p. 2719-2012.

Liao H.W., Lee C.T., 2000, Landslides triggered by the Chi-Chi earthquake. ACRS. http://www.a-a-r-s.org/acrs/proceeding/ACRS2000/Papers/HM00-7.htm

Liao C., Liao H., Lee C., 2002, Statistical analysis of factors affecting landslides triggered by the 1999 Chi-Chi earthquake, Taiwan. American Geophysical Union, Fall Meeting. http://adsabs.harvard.edu/abs/2002AGUFM.H12D0951L

Lindsey E. O., Natsuaki R., Xu X., Shimada M., Hashimoto M., Melgar D., Sandwell D. T., 2015, Line-of-sight displacement from ALOS-2 interferometry: Mw7.8 Gorkha Earthquake and Mw7.3 aftershock. Geophysics Res. Lett. v. 42, p. 6655–6661. doi:10.1002/2015GL065385

Martha, T.R., Kerle, N., vanWesten, C.J., Jetten, V., Kumar, K.V., 2012, Object-oriented analysis of multi-temporal panchromatic images for creation of historical landslide inventories. ISPRS journal of photogrammetry and remote sensing v. 67, p. 105-119.

McCalpin, J., 1984, Preliminary age classification of landslides for inventory mapping. Proceedings 21st annual Engineering Geology and Soils Engineering Symposium. University Press, Moscow, Idaho, p. 99–111.

Meunier P., Hovius N., Haines A.J., 2007, Regional patterns of earthquake-triggered landslides and their relation to ground motion. Geophysical Research Letter, v. 34(20), p. L20408
Moosavi, V., Talebi, A., Shirmohammadi, B., 2014, Producing a landslide inventory map using pixel-based and object-oriented approaches optimized by Taguchi method. Geomorphology 204, 646-656.

Mugnier, J. L., Leturmy, P., Mascle, G., Huyghe, P., Chalaron, E., Vidal, G., Husson, L., and Delcaillau, B. (1999). The Siwaliks of western Nepal 1: Geometry and kinematics. Journal Asian Earth Science v. 17, p. 629–642.

Nakata, T. (1989), Active faults of the Himalaya of India and Nepal, In “Tectonics of the Western Himalayas”. Geological Society of America, p. 243–264.

Nepal Ministry of Home Affairs, Government of Nepal and Disaster Preparedness Network Nepal, 2014, Nepal Disaster Report 2013

Parameswaran R. M., Natarajan T., Rajendran K., Rajendran C. P., Mallick R., Wood M., Lekhak H. C., 2015, Seismotectonics of the April–May 2015 Nepal earthquakes: An assessment based on the aftershock patterns, surface effects and deformational characteristics. J. Asian Earth Sci. v. 111, p. 161–174, doi:10.1016/j.jseaes.2015.07.030

Parise M., Jibson R.W., 2000, A seismic landslide susceptibility rating of geologic units based on analysis of characteristics of landslides triggered by the 17 January, 1994 Northridge, California earthquake. Engineering Geology, v. 58(3–4), p. 251–270

Parker, R.N., Densmore, A.L., Rosser, N.J., de Michele, M., Li, Y., Huang, R.Q., Whadcoat, S., Petley, D.N., 2011, Mass wasting triggered by the 2008 Wenchuan earthquake is greater than orogenic growth. Nature Geoscience v. 4, p. 449-452.

Pašek, J., 1975, Landslide inventory. International Association Engineering Geologist Bulletin v. 12, p. 73–74.

Patriat, P., and J. Achache, 1984, India-Eurasia collision chronology has implications for crustal shortening and driving mechanisms of plates. Nature v. 311, p. 615-621.

Powell, C. M. A., and Conaghan, P. J., 1973, Plate tectonics and the Himalayas: Earth Planetary Science Letters v. 20, p. 1–12.

Rana, B.J.B., 1935, Nepal Ko Maha Bhukampa (Great Earthquake of Nepal), Jorganesh Press.

Ratschbacher, L., Frisch,W., Liu, G., and Chen, C., 1994, Distributed deformation in southern and western Tibet during and after India-Asia collision. Journal of Geophysical Research, v. 99, p. 19917–19945.

Robinson, D. M., DeCelles, P. G., Patchett, P. J., Garzione, C. N. 2001, The kinematic history of the Nepalese Himalaya interpreted from Nd isotopes. Earth and Planetary Science Letters, v. 192, p. 507-521.

Robinson D.M., Pearson O.N., 2006, Exhumation of Greater Himalayan rock along the Main Central thrust, Nepal: Implications for channel flow. *in* Law R.D., Searle M.P., Godin L., *eds.,* Channel Flow, Extrusion, and Exhumation in Continental Collision Zones. Geological Society of London Special Publication v. 268, p. 255–268.

Rowley, D. B., 1996, Age of initiation of collision between India and Asia: A review of stratigraphic data. Earth and Planetary Science Letters v. 145, p. 1-13.

Sato, H. P., Harp, E. L., 2009, Interpretation of earthquake-induced landslides triggered by the 12 May 2008, M7.9 Wenchuan earthquake in the Beichuan area, Sichuan Province, China using satellite imagery and Google Earth. Landslides v. 6, p. 153-159

Searle, M., Corfield, R. I., Stephenson, B., and McCarron, J., 1997, Structure of the north Indian continental margin in the Ladakh-Zanskar Himalayas: Implications for the timing of obduction of the Spontang ophiolite, India-Asia collision and deformational events in the Himalaya. Geological Magazine, v. 134, p. 297–316.

Seeber, L. and Armbruster, J.G., 1984, Some elements of continental subduction along the Himalayan front: Lithosphere: Structure, Dynamics and Evolution. Tectonophysics v. 105, p. 263–278.

Tiwari, B., and Marui, H. 1998. Landslide investigation and prevention practice in Nepal. Annual report of Research Institute for Hazards in Snowy Areas, 20, 37-55. Nepal Ministry of Home Affairs. 2014. Nepal Disaster Report 2013.

Wieczorek, G.F., 1984, Preparing a detailed landslide-inventory map for hazard evaluation and reduction. Bulletin of the Association of Engineering Geologists v. 21, p. 337–342.

Xu, C., Xu, X.W., 2012a, Comment on "Spatial distribution analysis of landslides triggered by 2008.5. 12 Wenchuan earthquake, China" by Shengwen Qi, Qiang Xu, Hengxing Lan, Bing Zhang, Jianyou Liu. Engineering Geology v. 116 (2010), 95-108. Engineering Geology v. 133, p. 40-42.

Xu, C., Xu, X.W., 2012b, Spatial distribution of seismic landslides and their erosion thickness relate with a transpressional fault caused earthquake of subduction zone. Journal of Engineering Geology v. 20, p. 732-744 (in Chinese).

Xu, C., Xu, X.W., Yu, G.H., 2013, Landslides triggered by slipping-fault-generated earthquakes on a plateau: an example of the 14 April 2010, M_S 7.1, Yushu, China earthquake. Landslides v. 10 (4), p. 421-431.

Xu, C., Xu, X., Shyu. J. B. H., Zheng. W., Min. W., 2014a, Landslides triggered by the 22 July 2013 Minxian-Zhangxian, China, Mw 5.9 earthquake: Inventory compiling and spatial distribution analysis. Journal of Asian Earth Sciences v. 92, p. 125-142

Xu, C., Xu, X.W., Yao, X., Dai, F.C., 2014b. Three (nearly) complete inventories of landslides triggered by the May 12, 2008 Wenchuan Mw 7.9 earthquake of China and their spatial distribution statistical analysis. Landslides v. 11, p. 441-461.

Xu C., 2015, Preparation of earthquake-triggered landslide inventory maps using remote sensing and GIS technologies: Principles and case studies. Geoscience Frontiers v. 6, p. 825-836.

Yeats, R. S., Nakata, T., Farah, A., Mizra, M. A., Pandey, M. R., and Stein, R. S., 1992, The Himalayan frontal fault system. Annales Tectonicae, Special Issue (Supp. to Vol. 6), p. 85–98.